MOX-Report No. 11/2023

A parallel well-balanced numerical scheme for the simulation of fast landslides with efficient time stepping

Gatti, F.; de Falco, C.; Perotto, S.; Formaggia, L.

MOX, Dipartimento di Matematica
Politecnico di Milano, Via Bonardi 9 - 20133 Milano (Italy)

mox-dmat@polimi.it https://mox.polimi.it

A Parallel Well-balanced Numerical Scheme for the Simulation of Fast Landslides with Efficient Time Stepping

Federico Gatti[a], Carlo de Falco[a], Simona Perotto[a], Luca Formaggia[a]

[a]*MOX – Modelling and Scientific Computing, Department of Mathematics, Politecnico di Milano, Milan, Italy*

Abstract

We consider a single-phase depth-averaged model for the numerical simulation of fast-moving landslides with the goal of constructing a well-balanced, yet scalable and efficient, second-order time-stepping algorithm. We apply a Strang splitting approach to distinguish between parabolic and hyperbolic problems. For the parabolic contribution, we adopt a second-order Implicit-Explicit Runge-Kutta-Chebyshev scheme, while we use a two-stage Taylor discretization combined with a path-conservative strategy, to deal with the purely hyperbolic contribution. The proposed strategy allows to combine these schemes in such a way that the corresponding absolute stability regions remain unbiased, while guaranteeing positivity-preserving of the free surface and the well-balancing property to the overall implementation. The spatial discretization we adopt is based on a standard finite element method, associated with a hierarchically refined Cartesian grid. After providing numerical evidence of the well-balancing property, we demonstrate the capability of the proposed approach to select time steps larger with respect to the ones adopted by a classical Taylor-Galerkin scheme. Finally, we provide some meaningful scaling results, both on ideal and realistic scenarios.

Keywords:
Taylor-Galerkin scheme, Depth-integrated models, Implicit-explicit Runge-Kutta-Chebyshev scheme, C-property, Path-conservative methods, Parallel simulations.

1. Introduction

The two-step Taylor-Galerkin (TG2) method, introduced in [1, 2, 3], has been recently applied to the simulation of fast landslides [4, 5]. TG2 coincides with an explicit scheme. Consequently, it can be efficiently implemented in a parallel framework, yet it could require a too restrictive time step when compared with the

landslide run-out time-scale. This is due to the stiffness of the parabolic part and of the source characterizing the landslide model.

In this paper, we propose a new method that enables to use larger time steps with respect to the explicit TG2 scheme, while preserving the data locality property, which represents a key aspect for the implementation of a highly scalable code (see, e.g., [6]). More precisely, we set a second-order space-time numerical framework that enlarges the absolute stability region, while maintaining the locality of the implementation in order to efficiently solve the single-phase depth-integrated model for fast landslides. For the time discretization, the new method merges the second order Implicit–Explicit Runge–Kutta–Chebyshev (IMEX-RKC) scheme with a TG2 approach enriched by a path-conservative (PC) procedure (namely, a TG2-PC approximation), by resorting to a Strang splitting scheme [7, 8]. This choice allows us to integrate the non-conservative products so that the well-balance property is guaranteed. We resort to finite elements on hierarchical quadree meshes for the spatial discretization. This leads to approximate the diffusion-reaction contribution with a finite element IMEX-RKC scheme and the transport term with the TG2-PC method. The complete scheme will be referred to as Split IMEX-RKC TG2-PC method.

Concerning PC methods, the basic theory has been formalized by G. Dal Maso, P.C. Lefloch and F. Murat [9] on weak solutions to hyperbolic partial differential equations with non-conservative products, and successively developed by C. Parés, M.J. Castro and co-workers in the framework of a finite-volume discretization [10, 11, 12, 13, 14, 15, 16, 17, 18]. In particular, in the approximation of shallow water equations, it has been demonstrated that PC methods guarantee a well-balanced numerical scheme [19, 20]. The PC strategy has been already successfully employed in the literature in the context of a discontinuous Galerkin (DG) spatial discretization, see [21, 22]. On the contrary, to the authors knowledge, the PC scheme has been never adopted in a continuous finite element setting. In the verification phase, we provide numerical evidence of the capability of PC schemes to satisfy the well-balance property also when dealing with a continuous finite element approximation.

With reference to the IMEX-RKC method, the approach was introduced in [23] as an extension of the Runge–Kutta–Chebyshev (RKC) method first proposed in [24], and successfully used in reaction-diffusion problems (see, e.g., [25, 26, 27]). IMEX-RKC treats the moderately stiff diffusion terms explicitly and the strongly nonlinear reaction terms implicitly. The explicit treatment of the diffusion term is a key aspect in a parallel implementation since an implicit treatment needs to solve a global linear system and creates a potential bottleneck in the parallel implementation. In this work, we propose an implementation of the IMEX-RKC approach in a finite element space associated with a quadtree partition of the computational

domain. This constitutes a novelty with respect to the state-of-the-art, where such a scheme is, in general, adopted in a conforming discrete setting.

The paper is organized as follows. In Section 2 we present the single-phase depth-integrated mathematical model for fast landslides. Section 3 illustrates the Split IMEX-RKC TG2-PC method, first by describing the TG2-PC and the IMEX-RKC schemes we adopt and successively by dealing with the Strang split procedure. In Section 4, we analyze the reliability of the Split IMEX-RKC TG2-PC scheme through some numerical checks. In particular, after investigating the accuracy of the procedure, we show numerical evidence of the well-balancing property together with the capability to use a larger time step when compared with a basic TG2 scheme. Then, we assess the performance of the overall parallel implementation by performing a strong scalability analysis on both ideal and real satellite orography. Concluding remarks are provided in Section 5.

2. Model equations

Let us consider a rectangular computational domain, $\Omega \subset \mathbb{R}^2$, which contains a subdomain, $\Omega_w \subset \Omega$, representing the region of landslide material, varying in space and time, defined as the portion of Ω where the depth, H, of the landslide material is strictly greater than zero.

We are interested in solving the following set of nonlinear and non-conservative equations,

$$\partial_t \mathbf{q} + \nabla \cdot \mathbf{F} + \nabla \cdot \mathbf{G} + \mathbf{B}\nabla Z = \mathbf{r} \quad \text{in } \Omega_w \times (0, T], \tag{1}$$

equipped with proper boundary and initial conditions, where $\mathbf{q} = \mathbf{q}(\mathbf{x}, t) \in \mathbb{R}^4$ is the vector of conserved variables, $\mathbf{F} = \mathbf{F}(\mathbf{q}) \in \mathbb{R}^{4\times 2}$ is the tensor of transport fluxes, $\mathbf{G} = \mathbf{G}(\mathbf{q}, \nabla\mathbf{q}) \in \mathbb{R}^{4\times 2}$ is the tensor of diffusive fluxes, $\mathbf{B} = \mathbf{B}(\mathbf{q}) \in \mathbb{R}^{4\times 2}$ is the matrix of the non-conservative terms, Z is the orography profile, $\mathbf{r} = \mathbf{r}(\mathbf{q}) \in \mathbb{R}^4$ is the reaction term, and $(0, T]$ denotes the time window of interest. In particular, to model the landslide run-out phase, we consider the de Saint-Venant equations (see, e.g., [28, 29, 5, 30]), so that $\mathbf{q} = [H, U_x, U_y, Z]^T$, with x- and y-direction mass fluxes U_x and U_y, respectively. In more detail, the transport fluxes

coincide with

$$\mathbf{F}(\mathbf{q}) = \begin{bmatrix} U_x & U_y \\ \dfrac{U_x^2}{H} + \dfrac{1}{2} g H^2 & \dfrac{U_y U_x}{H} \\ \dfrac{U_y U_x}{H} & \dfrac{U_y^2}{H} + \dfrac{1}{2} g H^2 \\ 0 & 0 \end{bmatrix}, \tag{2}$$

with g the gravitational field; the diffusive fluxes are characterized by the expressions

$$\mathbf{G}(\mathbf{q}, \nabla \mathbf{q}) = \begin{bmatrix} 0 & 0 \\ -\dfrac{1}{\rho}\sigma_{xx} H & -\dfrac{1}{\rho}\sigma_{xy} H \\ -\dfrac{1}{\rho}\sigma_{xy} H & -\dfrac{1}{\rho}\sigma_{yy} H \\ 0 & 0 \end{bmatrix}, \tag{3}$$

with ρ the material density that we assume uniform and constant, and where the set $\{\sigma_{ij}\}_{ij}$, $i, j = x, y$, defines the deviatoric part of the Cauchy stress tensor $\boldsymbol{\sigma}$; the non-conservative matrix is defined by

$$\mathbf{B}(\mathbf{q}) = \begin{bmatrix} 0 & 0 \\ gH & 0 \\ 0 & gH \\ 0 & 0 \end{bmatrix}; \tag{4}$$

the reaction term is given by

$$\mathbf{r}(\mathbf{q}) = \begin{bmatrix} 0 \\ \dfrac{1}{\rho} f_x^B \\ \dfrac{1}{\rho} f_y^B \\ 0 \end{bmatrix}, \tag{5}$$

with $f_i^B = f_i^B(\mathbf{q})$, $i = x, y$, the bed friction. In particular, we adopt the Voellmy rheology, i.e., we choose

$$f_i^B(\mathbf{q}) = -\left(p_b \tan\delta \, \mathrm{sgn} w_i + \rho g \frac{|w_i| w_i}{\xi} \right), \tag{6}$$

being $\mathbf{w}$ the velocity field with components $w_i = U_i/H$, $i = x, y$ and sgn the signum function. The p_b is the basal pressure and according to Stevino varies linearly along the vertical axis, i.e., $p_b = p_s + \rho g H$ with p_s the atmospheric pressure, δ is the bed friction angle that we assume constant in time due to the absence of consolidation processes in the considered model, and ξ is the turbulence coefficient.

Concerning the tensor $\boldsymbol{\sigma}$, following the works [31, 29, 32], we adopt a depth-integrated regularized visco-plastic Bingham stress model where the regularization is performed through an exponential function. Thus, we have

$$\boldsymbol{\sigma} = \left(2\mu + \frac{\tau_Y (1 - e^{-N\sqrt{I_2}})}{\sqrt{I_2}} \right) \mathbf{D}, \tag{7}$$

where μ is the fluid viscosity, τ_Y is the yield shear stress, N is the regularization parameter, $\mathbf{D}$ is the horizontal strain rate tensor defined by $\mathbf{D} = \frac{1}{2}(\nabla \mathbf{w} + \nabla \mathbf{w}^T)$, and I_2 is the second invariant of the complete depth-integrated strain tensor and is calculated following a procedure fully described in the works [5, 6].
The regularization parameter N (set to $1000s$ in all the simulations of Section 4, as in [32]) is necessary to prevent the deviatoric stress tensor from becoming singular in the case of low strain rates, i.e., when the second invariant is close to zero. This implies that, in the limit of I_2 close to zero, the exponentially regularized rheology exists finite and is proportional to the coefficient N, that is, the apparent viscosity that multiplies the tensor $\mathbf{D}$ in (7) becomes equal to $\bar{\mu} = 2\mu + N\tau_Y$.

Finally, we point out that the model (1) admits the steady state 'lake-at-rest' solution [33], i.e.,

$$\eta = H + Z = \text{constant}, \quad [U_x, U_y]^T = \mathbf{0}, \tag{8}$$

where η is the free surface height. In the rest of the paper, we will refer to a well-balanced numerical method when it can ensure the lake-at-rest solution (see Section 4.1.2). We note that, the lake-at-rest condition leads to a balance between pressure forces and slope contributions, namely to satisfy the condition

$$\text{wb} = \nabla \cdot \mathbf{F} + \mathbf{B} \nabla Z = \mathbf{0} \tag{9}$$

in the whole domain.

3. The numerical scheme

Before considering the specific discretization we adopt, it is important to remark that model (1) is actually approximated on the whole computational spatial domain Ω rather than on the wet region Ω_w only. With this aim, we introduce a threshold $H_{\min}$ for the depth of the landslide material, under which we assign a null velocity, thus defining the wet (dry) region as the portion of Ω where $H > H_{\min}$ ($H \leq H_{\min}$). This modeling trick considerably simplifies the numerical treatment of problem (1), since domain Ω_w varies in time and can take any possible shape; vice versa domain Ω does coincide with a rectangle during the entire time window. This leads to the imposition of boundary conditions directly on the boundary of the computational domain, $\partial\Omega$, rather than on the wet-dry interface curve $\partial\Omega_w$ changing in time.

This wetting-drying method is fully conservative since drainage zones are explicitly identified. Moreover, on the wet-dry interface, outflow or zero mass flux boundary conditions are automatically imposed, depending on the local orography profile. The wetting-drying approach is thoroughly described in [34], where it is applied to the numerical solution of the semi-Lagangian shallow water equations when resorting to a DG space discretization.

In the next two sections, we introduce the numerical schemes which turn out to be instrumental in the formalization of the Split IMEX-RKC TG2-PC method proposed in this paper, see Section 3.3.

3.1. The TG2-PC scheme

The two-step Taylor-Galerkin (TG2) scheme is based on a Taylor series expansion in time which, according to [35], offers a useful alternative to a Runge-Kutta time integration when dealing with non-stiff problems. Indeed, a TG2 scheme requires to perform a flux limiting procedure just once per time step, in contrast to a Runge-Kutta method which demands such a correction at each stage of the method.

In this paper, we propose a new variant to the standard explicit TG2 scheme by introducing the integration of the non-conservative contributions with a PC method. For a review of the explicit standard TG2 scheme in fast landslide simulation, we refer to [36, 6].

Let us consider a hyperbolic problem with non-conservative contributions, i.e., model (1) when omitting the diffusive fluxes $\mathbf{G}$ and the source term $\mathbf{r}$. This is equivalent to considering frictionless shallow-water equations in the presence of an arbitrary bottom, which is fixed in time (i.e., with $\partial_t Z = 0$).
At a generic time t^{n+o}, $o = 0, \frac{1}{2}, 1$, after denoting by $\mathbf{Q}^{n+o} \approx \mathbf{q}^{n+o}$ the time

discrete counterpart of the conservative variable at time t^{n+o}, and letting $\mathbf{F}^{n+o} = \mathbf{F}(\mathbf{Q}^{n+o})$, $\mathbf{B}^{n+o} = \mathbf{B}(\mathbf{Q}^{n+o})$, we integrate system (1) between two consecutive time instants, t^n and t^{n+1}. This yields the two-step second-order semi-discrete scheme,

$$\begin{cases} \mathbf{Q}^{n+\frac{1}{2}} = \mathbf{Q}^n + \dfrac{\Delta t}{2}\left(-\nabla\cdot\mathbf{F}^n - \mathbf{B}^n\nabla Z^n\right), \\ \mathbf{Q}^{n+1} = \mathbf{Q}^n + \Delta t\left[-\nabla\cdot\mathbf{F}^{n+\frac{1}{2}} - \mathbf{B}^{n+\frac{1}{2}}\nabla Z^{n+\frac{1}{2}}\right], \end{cases} \tag{10}$$

where the first equation coincides with a first-order predictor step used to provide an approximation of the conservative variables at the intermediate time.

Now, we consider discretization in space by using the finite element method to recover the fully discrete scheme. We partition domain Ω by means of a family, $\{\mathcal{D}_h\}$, of quadrilateral structured meshes with spacing h. We associate with $\mathcal{D}_h$ two discrete spaces, namely the space $\mathbb{Q}_0$ of the (discontinuous) piece-wise constant polynomials to discretize the first step in (10), and the space $\mathbb{Q}_1$ of the continuous piece-wise bilinear polynomials for the discretzation of the second step. In particular, $\mathbf{Q}^{n+\frac{1}{2}}$ is approximated in space $\mathbb{Q}_0$, while both $\mathbf{Q}^n$ and $\mathbf{Q}^{n+1}$ are chosen in $\mathbb{Q}_1$. Spaces $\mathbb{Q}_0$ and $\mathbb{Q}_1$ are endowed with a basis, given by $\{\phi_j^{(0)}, j = 1,\dots,M\}$ and $\{\phi_i^{(1)}, i = 1,\dots,N\}$, respectively, after denoting by M the number of quadrilateral elements in $\mathcal{D}_h$ and by N the number of mesh nodes. Thus, the fully-discrete weak form reads

$$\begin{aligned} (\mathbf{Q}^{n+\frac{1}{2}}, \phi_j^{(0)}) &= (\mathbf{Q}^n, \phi_j^{(0)}) - \frac{\Delta t}{2}(\nabla\cdot\mathbf{F}^n, \phi_j^{(0)}) - \frac{\Delta t}{2}(\mathbf{B}^n\nabla Z^n, \phi_j^{(0)}), \\ (\mathbf{Q}^{n+1}, \phi_i^{(1)}) &= (\mathbf{Q}^n, \phi_i^{(1)}) + \Delta t\,(\mathbf{F}^{*,n+\frac{1}{2}}, \nabla\phi_i^{(1)}) - \Delta t\,(\mathbf{B}^{n+\frac{1}{2}}\nabla Z^{n+\frac{1}{2}}, \phi_i^{(1)}), \end{aligned} \tag{11}$$

for $j = 1,\dots,M$, $i = 1,\dots,N$, where $(\cdot,\cdot)$ indicates the $L^2(\Omega)$-scalar product, while $\mathbf{F}^{*,n+\frac{1}{2}}$ is a discretization flux that we define below and $\mathbf{n}$ is the outward unit normal vector to the domain Ω. We note that, in this fully discrete weak-form, we have neglected the boundary integrals to be computed on the boundary of the computational domain $\partial\Omega$, i.e. the integral $\int_{\partial\Omega}\mathbf{F}^{*,n+\frac{1}{2}}\,\mathbf{n}\,\phi_i^{(1)}\,d\Sigma$. It is over there that we apply boundary conditions. A complete study of boundary conditions for hyperbolic problems is beyond the study of the present work, here we consider non-reflecting boundary conditions, the reader can refer e.g. to [37] for details. Following the work [38], in the second step of the Equation (11) we rely on the mass lumping technique to avoid the inversion of the consistent mass matrix. This choice makes the method particularly suited to a parallel implementation since

each computation in the second step can be performed node-wise. Moreover, we highlight two further difficulties related to the computation of this step, i.e., the evaluation of the integral of the non-conservative product and the design of a high-order discretization flux, able to ensure both the well-balancing and the positivity-preserving property.

Let us focus on the former issue. We rely on the PC theory that is able to provide an analytical meaningful interpretation of the non-conservative products in a weak sense [10]. The adoption of a PC approach allows us to modify the scheme to ensure the well-balancing property by selecting an appropriate path. Even if the PC strategy has been widely applied in the literature in discrete settings like in the context finite volumes [19, 39] and DG discretizations [40], to the authors knowledge it has never been applied in a continuous finite element setting and especially in the framework of the TG2 scheme. Here, we provide an application in the continuous finite element space. It is worth noting that the PC method could suffer from controversial aspects. This has been widely addressed in [41] where the authors show that the PC method is not always capable to reproduce the solution expected by the conservative numerical solver.
We define a path

$$\Psi = \Psi(Z_-^{n+\frac{1}{2}}, Z_+^{n+\frac{1}{2}}, s) = Z_-^{n+\frac{1}{2}} + s(Z_+^{n+\frac{1}{2}} - Z_-^{n+\frac{1}{2}}), \tag{12}$$

which connects two orography states, $Z_-^{n+\frac{1}{2}}$ and $Z_+^{n+\frac{1}{2}}$, related to two mesh elements sharing the same edge e, with s the parameter spanning the path, for $0 \leq s \leq 1$. We choose a standard linear path. As stated in [20], the motivation behind the specific choice of the path is the simplicity, together with the fact that the path is expected to guarantee the resulting scheme to be exactly well-balanced for water at rest solutions of shallow-water type equations. Let us call $\mathcal{E}_i$ the set of the edges e that share the node i. Then, the PC nodal formulation for the non-conservative product in the second step of (11) becomes

$$(\mathbf{B}^{n+\frac{1}{2}} \nabla Z^{n+\frac{1}{2}}, \phi_i^{(1)}) = \sum_{e \in \mathcal{E}_i} \int_e \phi_i^{(1)} dl \int_0^1 \mathbf{B}\big(\Psi(Z_-^{n+\frac{1}{2}}, Z_+^{n+\frac{1}{2}}, s)\big) \mathbf{n}_e \, \partial_s \Psi ds, \tag{13}$$

where $\mathbf{n}_e$ is the unit normal to the edge, such that $\mathbf{n}_e \cdot (\mathbf{x}_+ - \mathbf{x}_-) > 0$ with $\mathbf{x}_+$ and $\mathbf{x}_-$ the coordinates of the barycenter of two elements sharing edge e, while $\partial_s \Psi$ denotes the derivative along the selected path. Finally, the two integrals are numerically computed with the trapezoidal quadrature rule.

Proposition 3.1. *The fully discrete weak-form appearing in Equation* (11) *with the non-conservative products appearing in the second step of the method computed*

with Equation (13) *is exact in the modeling of the lake-at-rest condition, at the discrete level.*

Proof. A numerical method then is called well-balanced if it satisfies at the discrete level the Equation (9). To simplify the presentation, we prove that the well-balancing condition is satisfied by illustrating what happens just for the material height and for the momentum equation along the x-direction. For this reason, we consider a one-dimensional motion in a two-dimensional domain.
Moreover, we make notation easier by neglecting the temporal index in the discrete variables. Thus, a discrete quantity associated with the barycenter of a quadrilateral cell refers to time $t^{n+\frac{1}{2}}$ and belongs to space $\mathbb{Q}_0$. A discrete quantity associated with a node refers to time t^n and belongs to space $\mathbb{Q}_1$. To make an example, $H_{i,j}$ denotes the space-time discrete counterpart of the material height, H, at the node with coordinates (i, j) and at time t^n, while one-half coordinates, such as $(i+\frac{1}{2}, j+\frac{1}{2})$, identify the degrees of freedom characterizing the space $\mathbb{Q}_0$ at time $t^{n+\frac{1}{2}}$. In particular, the discrete well-balancing equation at the generic coordinate (i, j) will be denoted by $\mathrm{WB}^{H}_{(i,j)}$ for the material height and by $\mathrm{WB}^{U_x}_{(i,j)}$ for the mass flux along the x-direction.

We start by considering the first step of the TG2-PC method. We take a quadrilateral element with extension $\Delta x \times \Delta y$ and we compute the one-half solution $\mathbf{Q}^{n+\frac{1}{2}}$ at the node with coordinates $(i+\frac{1}{2}, j+\frac{1}{2})$ (see Figure 1). We denote by

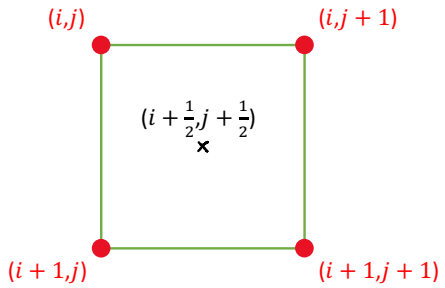

Figure 1: Quadrilateral element centered at $(i+\frac{1}{2}, j+\frac{1}{2})$. The degrees of freedom associated with space $\mathbb{Q}_1$ are red-highlighted; the black cross (i.e., the barycenter of the quad) corresponds to the degree of freedom of the space $\mathbb{Q}_0$.

$H^{n,2}$ the square of the space-time discrete material height at time t^n, and we select it in $\mathbb{Q}_1$. By integrating exactly the balancing integrals in the first step of the TG2-PC method, we obtain the following well-balancing condition for the mass flux U_x at the node $(i+\frac{1}{2}, j+\frac{1}{2})$,

$$\mathrm{WB}^{U_x}_{i+\frac{1}{2},j+\frac{1}{2}} = \left(\frac{1}{2} g \partial_x H^{n,2}, \phi^{(0)}_{i+\frac{1}{2},j+\frac{1}{2}}\right) + \left(g H^n \partial_x Z^n, \phi^{(0)}_{i+\frac{1}{2},j+\frac{1}{2}}\right)$$

$$= \left(gH^n \partial_x H^n, \phi^{(0)}_{i+\frac{1}{2},j+\frac{1}{2}} \right) + \left(gH^n \partial_x Z^n, \phi^{(0)}_{i+\frac{1}{2},j+\frac{1}{2}} \right)$$

$$= \left(gH^n \partial_x (H^n + Z^n), \phi^{(0)}_{i+\frac{1}{2},j+\frac{1}{2}} \right) = 0. \tag{14}$$

This chain of equalities is obtained by exploiting the hypothesis of null mass flux $U_x^n = 0$ at time t^n, together with the relation $H^n + Z^n = \text{constant}$. These hypotheses are true since the generic time t^n does initially coincide with the initial condition. We can conclude that the first step of the TG2-PC scheme is exactly well-balanced. Indeed, considering again $U_x^n = 0$, one obtains $\text{WB}^H_{i+\frac{1}{2},j+\frac{1}{2}} = (\partial_x U_x^n, \phi^{(0)}_{i+\frac{1}{2},j+\frac{1}{2}}) = 0$. Moreover, we have exploited the fact that we can compute the spatial partial derivative in the element with cell center $(i + \frac{1}{2}, j + \frac{1}{2})$ since functions in $\mathbb{Q}_1$ are linear with respect to the spatial coordinates. In this way, the first step of the TG2-PC method does not add any particular complication and serves just as an input to the second step, according to a predictor/corrector paradigm [22, 21].

We now check whether the well-balancing property is satisfied in the second step of the TG2-PC scheme. To this aim, we consider the four elements with extension $\Delta x \times \Delta y$ sharing the generic internal node (i, j) (see Figure 2), where internal means that it is not a boundary node (i.e., it does not belong to $\partial\Omega$). We compute the value of the updated solution $\mathbf{Q}^{n+1}$ at node (i, j). In particular, in the figure, we identify in magenta the edges where we compute the PC integral. Denoting

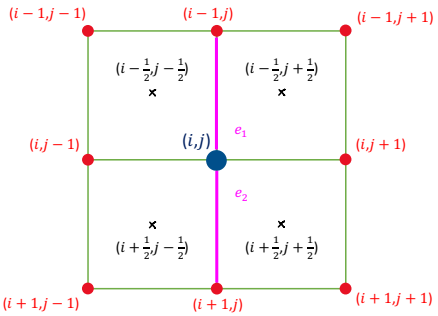

Figure 2: Elements sharing node (i, j) (in blue). The other degrees of freedom associated with space $\mathbb{Q}_1$ are red-highlighted; the degrees of freedom of space $\mathbb{Q}_0$ are depicted with the black cross. Two edges e_1, e_2 are highlighted in magenta needed for the PC method.

by $H^{n+\frac{1}{2},2}$ the square of the space-time discrete quantity $H^{n+\frac{1}{2}}$ belonging to $\mathbb{Q}_0$ and at time $t^{n+\frac{1}{2}}$, after integrating exactly the conservative flux and by using the trapezoidal rule to integrate the PC formulation for the continuous space $\mathbb{Q}_1$, we

obtain the following well-balancing property at the discrete level,

$$
\begin{aligned}
\mathrm{WB}_{i,j}^{U_x} &= \left(\frac{1}{2}gH^{n+\frac{1}{2}},{}^{2}, \partial_x \phi_{i,j}^{(1)}\right) - \left(gH^{n+\frac{1}{2}}\partial_x Z^{n+\frac{1}{2}}, \phi_{i,j}^{(1)}\right) \\
&= \int_0^{\Delta x}\int_0^{\Delta y} \frac{1}{\Delta x}\frac{y}{\Delta y}\frac{1}{2}gH^2_{i+\frac{1}{2},j-\frac{1}{2}}dxdy \\
&+ \int_0^{\Delta x}\int_0^{\Delta y} \frac{-1}{\Delta x}\frac{y}{\Delta y}\frac{1}{2}gH^2_{i+\frac{1}{2},j+\frac{1}{2}}dxdy \\
&+ \int_0^{\Delta x}\int_0^{\Delta y} \frac{1}{\Delta x}\left(1-\frac{y}{\Delta y}\right)\frac{1}{2}gH^2_{i-\frac{1}{2},j-\frac{1}{2}}dxdy \\
&+ \int_0^{\Delta x}\int_0^{\Delta y} \frac{-1}{\Delta x}\left(1-\frac{y}{\Delta y}\right)\frac{1}{2}gH^2_{i-\frac{1}{2},j+\frac{1}{2}}dxdy \\
&- \sum_{k=1,2}\int_{e_k}\frac{1}{2}dy\int_0^1 gH^{n+\frac{1}{2}}\left(\Psi(s)\right)\partial_s\Psi ds \\
&= \frac{\Delta y}{2}\left(\frac{1}{2}gH^2_{i-\frac{1}{2},j-\frac{1}{2}} + \frac{1}{2}gH^2_{i+\frac{1}{2},j-\frac{1}{2}}\right) \\
&- \frac{\Delta y}{2}\left(\frac{1}{2}gH^2_{i-\frac{1}{2},j+\frac{1}{2}} + \frac{1}{2}gH^2_{i+\frac{1}{2},j+\frac{1}{2}}\right) \\
&- \frac{\Delta y}{2}\frac{1}{2}g\left(H_{i-\frac{1}{2},j-\frac{1}{2}} + H_{i-\frac{1}{2},j+\frac{1}{2}}\right)\left(Z_{i-\frac{1}{2},j+\frac{1}{2}} - Z_{i-\frac{1}{2},j-\frac{1}{2}}\right) \\
&- \frac{\Delta y}{2}\frac{1}{2}g\left(H_{i+\frac{1}{2},j-\frac{1}{2}} + H_{i+\frac{1}{2},j+\frac{1}{2}}\right)\left(Z_{i+\frac{1}{2},j+\frac{1}{2}} - Z_{i+\frac{1}{2},j-\frac{1}{2}}\right) \\
&= \frac{1}{2}g\frac{\Delta y}{2}\left(H_{i-\frac{1}{2},j-\frac{1}{2}} + H_{i-\frac{1}{2},j+\frac{1}{2}}\right)\left(H_{i-\frac{1}{2},j-\frac{1}{2}} + Z_{i-\frac{1}{2},j-\frac{1}{2}}\right) \\
&- \frac{1}{2}g\frac{\Delta y}{2}\left(H_{i-\frac{1}{2},j-\frac{1}{2}} + H_{i-\frac{1}{2},j+\frac{1}{2}}\right)\left(H_{i-\frac{1}{2},j+\frac{1}{2}} + Z_{i-\frac{1}{2},j+\frac{1}{2}}\right) \\
&+ \frac{1}{2}g\frac{\Delta y}{2}\left(H_{i+\frac{1}{2},j-\frac{1}{2}} + H_{i+\frac{1}{2},j+\frac{1}{2}}\right)\left(H_{i+\frac{1}{2},j-\frac{1}{2}} + Z_{i+\frac{1}{2},j-\frac{1}{2}}\right) \\
&- \frac{1}{2}g\frac{\Delta y}{2}\left(H_{i+\frac{1}{2},j-\frac{1}{2}} + H_{i+\frac{1}{2},j+\frac{1}{2}}\right)\left(H_{i+\frac{1}{2},j+\frac{1}{2}} + Z_{i+\frac{1}{2},j+\frac{1}{2}}\right) = 0. \quad (15)
\end{aligned}
$$

We note that $\mathrm{WB}_{i,j}^{U_x}$ is zero at the discrete level, being the first step of the TG2-PC scheme well-balanced. Indeed, since the well-balancing condition is satisfied in the first step, we have $H_{\bar{i},\bar{j}}+Z_{\bar{i},\bar{j}} =$ constant for $\bar{i} = i-\frac{1}{2}, i+\frac{1}{2}$ and $\bar{j} = j-\frac{1}{2}, j+\frac{1}{2}$ that

causes $\mathrm{WB}_{i,j}^{U_x}$ to be zero. In addition, since we do not have any non-conservative products in the mass equation, we trivially get $\mathrm{WB}_{i,j}^{H} = (U_x^{n+\frac{1}{2}}, \partial_x \phi_{i,j}^{(1)}) = 0$, which is satisfied thanks to the well-balancing property of the first step. This is sufficient to prove that the well-balancing condition is satisfied also at the second step of the TG2-PC method. To obtain expression (15), we have assumed a null momentum flux at time $t^{n+\frac{1}{2}}$, being the first step of the numerical scheme exactly well-balanced; moreover, we have used the algebraic relation $a^2 - b^2 = (a+b)(a-b)$, with a, $b \in \mathbb{R}$.
Finally, we remark that we have omitted the Rusanov flux contribution. In general, this term might deteriorate the well-balancing property of the PC method. Thus, particular care has to be taken to design a diffusive flux able to preserve this condition (we refer to the end of Section 3.1 for more details). □

We now address the design of a high-order discretization flux $\mathbf{F}^{*,n+\frac{1}{2}}$. The TG2 scheme is neither monotone nor positivity-preserving, being second order space-time accurate [42]. Here, we adopt the Zalesak's multidimensional Flux Corrected Transport (FCT) (see [43, 44, 45] for more details), in order to prevent the rise of spurious oscillations near discontinuities, i.e., the Gibbs phenomenon, so to maintain an oscillation-free positivity-preserving physical solution. As already underlined in the work [6], to this aim we adopt the Rusanov first-order monotone discretization flux weighted by the correction flux-limiting coefficient. However, we remark that the FCT strategy does not preserve the well-balanced property of the numerical scheme. This is a common feature of flux limiters, which has been already addressed in the case of a DG discretization [46]. Below, we adopt a procedure similar to the one used in this work for the approximation of shallow water equations with a DG approach.
To formalize the adopted well-balanced FCT method, let us consider a single quadrilateral element, Q, of the domain discretization with resolution $\Delta x \times \Delta y$ and consider the variable $\mathbf{v} = \mathbf{U}\mathbf{q}$, with

$$\mathbf{U} = \begin{bmatrix} 1 & 0 & 0 & u \\ 0 & 1 & 0 & 0 \\ 0 & 0 & 1 & 0 \\ 0 & 0 & 0 & 0 \end{bmatrix} \tag{16}$$

and $u = u(H - H_{\min})$ the Heaviside step function. Then, the Rusanov anti-diffusive flux is defined as,

$$\delta \mathbf{F}_Q^n = \max_{(\frac{\Delta x}{\Delta t}, \frac{\Delta y}{\Delta t})} \frac{1}{2\Delta t} (\nabla \mathbf{V}^n, \phi_Q^{(0)}), \tag{17}$$

with $\phi_Q^{(0)}$ the $\mathbb{Q}_0$-basis function associated with element Q and $\mathbf{V}^n$ the time discrete counter-part of the variable $\mathbf{v}$, i.e., $\mathbf{V}^n = \mathbf{U}^n\mathbf{Q}^n$. The exact integration in (17) results in an anti-diffusive flux, coinciding with a linear function of the ratios $\frac{\Delta x}{\Delta t}$ and $\frac{\Delta y}{\Delta t}$. Thanks to the CFL condition, these ratios are upper bounded by the maximum simple wave speed modulus in Q, along the x- and y-direction, respectively. The simple waves correspond to the eigenvalues of the full semi-linear system, namely the system that contains both conservative and non-conservative contributions. Finally, the discrete flux in the element Q is given by

$$\mathbf{F}_Q^{*,n+\frac{1}{2}} = (\mathbf{F}_Q^{n+\frac{1}{2}} - \delta\mathbf{F}_Q^n) + \alpha_Q\delta\mathbf{F}_Q^n, \tag{18}$$

where $\alpha_Q \in \mathbb{Q}_0$ denotes the piece-wise constant FCT coefficient defined according to the well-known Zalesak procedure [43, 44, 45] (for the specific implementation, we refer to [6]). Considering that the Zalesak procedure provides a positivity-preserving approximation only if the low order scheme is positivity-preserving. In particular, for the low order discretization flux we are considering, the following proposition hold,

Proposition 3.2. *The low order TG2-PC scheme produces a positivity-preserving discretization of the free surface height.*

Proof. To consider the low order scheme, we set on the single element Q $\mathbf{F}_Q^{*,n+\frac{1}{2}} = \mathbf{F}_Q^{n+\frac{1}{2}} - \delta\mathbf{F}_Q^n$. To ease the presentation, as hypothesis we consider the case of a one-dimensional motion, i.e., we set U_y known and equal to zero. Further, we consider the same convention on the symbols as introduced to demonstrate the Proposition (3.1). By considering a bottom topography $Z(\mathbf{x}) = 0$, the TG2 scheme if applied to the frictionless shallow water equations, reads

$$\begin{aligned}
H_{i,j}^{n+1} &= H_{i,j}^n + \frac{\Delta t}{\Delta x}(U_{x,i-\frac{1}{2},j-\frac{1}{2}}^{n+\frac{1}{2}} - U_{x,i-\frac{1}{2},j+\frac{1}{2}}^{n+\frac{1}{2}}),\\
U_{x,i-\frac{1}{2},j-\frac{1}{2}}^{n+\frac{1}{2}} &= \frac{U_{x,i,j}^n + U_{x,i,j-1}^n}{2} + \frac{\Delta t}{2\Delta x}(F_{i,j-1}^n - F_{i,j}^n),\\
U_{x,i-\frac{1}{2},j+\frac{1}{2}}^{n+\frac{1}{2}} &= \frac{U_{x,i,j}^n + U_{x,i,j+1}^n}{2} + \frac{\Delta t}{2\Delta x}(F_{i,j}^n - F_{i,j+1}^n),
\end{aligned}$$

where $F = Hw_x^2 + \frac{1}{2}gH^2$. Then, the material height update reads,

$$\begin{aligned}
H_{i,j}^{n+1} = H_{i,j}^n(1 - w_{x,i,j}^{2,n}\bar{\nu}^2 - gH_{i,j}^n\frac{\bar{\nu}^2}{2})\\
+ H_{i,j-1}^n(w_{x,i,j-1}^{2,n}\frac{\bar{\nu}^2}{2} + gH_{i,j-1}^n\frac{\bar{\nu}^2}{4} + w_{x,i,j-1}^n\frac{\bar{\nu}}{2})
\end{aligned}$$

$$+ H^n_{i,j+1}(w^{2,n}_{x,i,j+1}\frac{\bar{\nu}^2}{2} + gH^n_{i,j+1}\frac{\bar{\nu}^2}{4} - w^n_{x,i,j+1}\frac{\bar{\nu}}{2}), \tag{19}$$

where $\bar{\nu} = \frac{\Delta t}{\Delta x}$ and it is linked to the nodal CFL number ν through the relation $\nu = \bar{\nu}\lambda$ where λ is the maximum eigenvalue in modulus. Regarding the λ, we omit the nodal subscript but it is the maximum nodal wave-speed. In the following, we omit any temporal superscript and spatial subscript to ease the presentation. After simple algebra we can conclude that the TG2 method is not positivity-preserving, indeed by recasting the last two lines in Equation (19), we obtain

$$\nu \pm \frac{w_x|w_x| + w_x c}{w_x^2 + c^2/2} \geq 0$$

to ensure positivity of the updated material height. Note that above we have omitted the subscripts for the velocity and for the celerity $c = \sqrt{gH}$. By considering that in the limit of high velocities the equation above reduces to

$$\nu \pm 1 \geq 0$$

we can conclude that the TG2 method is not positivity-preserving being the limit case $\nu \geq 1$ violating the classical stability constraint of the TG2 scheme.
If now we consider the extra numerical diffusion given by the Rusanov flux in Equation (17), we obtain that the low-order solution is positivity-preserving if the following conditions are satisfied

$$\begin{cases} 1 - w_x^2\bar{\nu}^2 - c^2\dfrac{\bar{\nu}^2}{2} - \nu & \geq 0, \\ w_x^2\dfrac{\bar{\nu}^2}{2} + c^2\dfrac{\bar{\nu}^2}{4} \pm w_x\dfrac{\bar{\nu}}{2} + \dfrac{\nu}{2} & \geq 0, \end{cases} \tag{20}$$

where again we have omitted any temporal superscript and spatial subscript for simplicity. After simple algebra and in the limit case of high velocities, we can simplify the second equation above as

$$\nu + 1 \pm w_x\frac{\nu}{\lambda} + \nu \geq 0, \tag{21}$$

by exploiting the fact that $\nu = \frac{\Delta t}{\Delta x}(|w_x| + c)$ we can conclude that the Equation (21) is always satisfied being c positive for hypothesis. Regarding the first line in Equation (20), by noting that the condition,

$$\nu^2 > \bar{\nu}^2(w_x^2 + c^2/2),$$

holds in every flow condition, we can state the following restrictive simplification of this equation,

$$1 - \nu^2 - \nu \geq 0, \tag{22}$$

that leads to the conditions on the CFL number,

$$\frac{-1-\sqrt{5}}{2} \leq \nu \leq \frac{-1+\sqrt{5}}{2}.$$

While the conditions on the left is always satisfied being it negative, the condition on the right provides a more restrictive condition with respect to the CFL number required by stability, indeed $\frac{-1+\sqrt{5}}{2} \approx 0.6$. This is however an estimation of the most restrictive positivity condition, if this condition is satisfied, thanks to the FCT strategy the method is able to produce a positivity-preserving second-order solution.

In the more general case of a non planar orography, the positivity-preserving property can be proved just on the nodal free surface height $\eta_{i,j}^{n+1}$. Thanks to a constant orography profile, i.e., $\partial_t Z(\mathbf{x}) = 0$, we can sum to the updated mass equation $H_{i,j}^{n+1}$ the quantity $Z_{i,j}^n$. This leads to an updated equation for the variable $\eta_{i,j}^{n+1}$. In particular, we can recognize two contributions, a first one, which has been already analyzed in the case of $Z(\mathbf{x}) = 0$, and another one, which is a function of the quantities $Z_{i,j-1}^n$, $Z_{i,j}^n$, $Z_{i,j+1}^n$. We report here the new contribution we call contr_2,

$$\text{contr}_2 = \frac{\bar{\nu}^2}{2}(Z_{i,j-1}^n \bar{c}_l^2 - Z_{i,j}^n(\bar{c}_l^2 + \bar{c}_r^2) + Z_{i,j+1}^n \bar{c}_r^2),$$

where $\bar{c}_l^2 = \frac{g(H_{i,j}^n + H_{i,j-1}^n)}{2}$, $\bar{c}_r^2 = \frac{g(H_{i,j}^n + H_{i,j+1}^n)}{2}$. By considering now the well-balancing correction of the limiter, i.e. the Equation (17), we note that the nodal free surface height results positive if the following condition on the coefficient multiplying $Z_{i,j}^n$ holds,

$$1 - \nu^2 - \nu \geq 0.$$

To obtain the inequality above we have exploit the fact that $\nu^2 \geq \frac{\Delta t^2}{2\Delta x^2}\bar{c}^2$. We note that we obtain the same condition obtained in case of null orography profile, i.e., the Equation (22).

□

3.2. The second order IMEX-RKC finite element scheme

To face the stiffness of the diffusion and source terms, we resort to a second order space-time Implicit–Explicit Runge–Kutta–Chebyshev (IMEX-RKC) finite element scheme. This method avoids to build a global matrix, as in case of implicit

schemes, while maintaining the node-wise operation structure suited to a parallel implementation.

With this aim, we start from a diffusion-reaction equation (i.e., we neglect the hyperbolic contribution in model (1) coinciding with the terms depending on $\mathbf{F}$ and $\mathbf{B}$), and we consider the corresponding spatial discretization based on the finite element space $\mathbb{Q}_1$ associated with the quadrilateral structured partition $\mathcal{D}_h$ of Ω,

$$\begin{cases} \frac{d}{dt}\mathbf{V}_i = \mathbf{F_D}(t, \mathbf{V}_{\mathcal{N}_i}) + \mathbf{F_R}(t, \mathbf{V}_i), \\ \mathbf{F_D}(t, \mathbf{V}_{\mathcal{N}_i}) = (\mathbf{G}, \nabla\phi_i^{(1)}), \\ \mathbf{F_R}(t, \mathbf{V}_i) = (\mathbf{r}, \phi_i^{(1)}), \end{cases} \tag{23}$$

for $i = 1, \ldots, N$, and where $\mathbf{V}_i = (\mathbf{q}, \phi_i^{(1)})$ is a vector function of time discretizing the conserved variable $\mathbf{q}$ at the node i, being the integral computed with a mass lumping approach. Accordingly, $\mathbf{F_D}(t, \mathbf{V}_{\mathcal{N}_i})$ and $\mathbf{F_R}(t, \mathbf{V}_i)$ provide the spatial discretizations of the diffusive fluxes and of the reaction term, respectively. The symbol $\mathbf{V}_{\mathcal{N}_i}$ denotes the discretizations of $\mathbf{q}$ in the set of nodes of the elements containing node i.
Finally, we note that, in this semi-discrete formulation, we have omitted the boundary conditions on the diffusive flux, we have set $\int_{\partial\Omega} \mathbf{G}\,\mathbf{n}\,\phi_i^{(1)}\, d\Sigma = \mathbf{0}$. Again, a complete treatment of boundary conditions, in this case for purely diffusive problems, is beyond the scope of the present work. We consider null boundary fluxes for simplicity and considering also that most of the influence is due to the transport fluxes in an advection dominated problem.

It is well-known that a spatial discretization through linear finite elements of the diffusive fluxes leads to a space-discrete operator whose eigenvalues lie on the real axis and are all negatives. To this aim we consider the IMEX-RKC time integration scheme [23]. Which is an extension of the RKC scheme designed for the time integration of diffusion problems [24] and that has been already applied in the framework of linear finite elements in the work [27]. The second-order IMEX-RKC scheme can be formalized in such a way: given the numerical solution $\mathbf{V}_i^n$ at

time t^n, the updated solution, $\mathbf{V}_i^{n+1}$, is computed by:

$$\left\{\begin{array}{rcl} \mathbf{W}_i^0 & = & \mathbf{V}_i^n, \\ \mathbf{W}_i^1 & - & \tilde{\mu}_1 \Delta t\, \mathbf{F}_{\mathbf{R}}^1(\mathbf{W}_i^1) = \mathbf{W}_i^0 + \tilde{\mu}_1 \Delta t\, \mathbf{F}_{\mathbf{D}}^0(\mathbf{W}_{\mathcal{N}_i}^0), \\ \mathbf{W}_i^j & - & \tilde{\mu}_1 \Delta t\, \mathbf{F}_{\mathbf{R}}^j(\mathbf{W}_i^j) = (1-\mu_j-\nu_j)\mathbf{W}_i^0 + \mu_j \mathbf{W}_i^{j-1} + \nu_j \mathbf{W}_i^{j-2} \\ & + & \tilde{\mu}_j \Delta t\, \mathbf{F}_{\mathbf{D}}^{j-1}(\mathbf{W}_{\mathcal{N}_i}^{j-1}) + \tilde{\gamma}_j \Delta t\, \mathbf{F}_{\mathbf{D}}^0(\mathbf{W}_{\mathcal{N}_i}^0) \\ & + & (\tilde{\gamma}_j \tilde{\mu}_1 \mu_j / \tilde{\mu}_j - (1-\mu_j-\nu_j)\tilde{\mu}_1) \Delta t\, \mathbf{F}_{\mathbf{R}}^0(\mathbf{W}_i^0) \\ & - & \nu_j \tilde{\mu}_1 \Delta t\, \mathbf{F}_{\mathbf{R}}^{j-2}(\mathbf{W}_i^{j-2}), \quad j = 2, \ldots, m, \\ \mathbf{V}_i^{n+1} & = & \mathbf{W}_i^m, \end{array}\right. \tag{24}$$

where $\mathbf{W}_i^0, \ldots, \mathbf{W}_i^m$ are intermediate vectors in the node i, fluxes $\mathbf{F}_{\mathbf{D}}^j(\mathbf{W}_{\mathcal{N}_i}^j)$, $\mathbf{F}_{\mathbf{R}}^j(\mathbf{W}_i^j)$ stand for $\mathbf{F}_{\mathbf{D}}(t^n + c_j \Delta t, \mathbf{W}_{\mathcal{N}_i}^j), \mathbf{F}_{\mathbf{R}}(t^n + c_j \Delta t, \mathbf{W}_i^j)$ respectively, with $0 = c_0 < c_1 < \cdots < c_m = 1$. Again, $\mathbf{W}_{\mathcal{N}_i}^j$ refers to the set of vectors $\mathbf{W}_k^j$, $k = 1, \ldots, N$ defined on the set of nodes belonging to the set of elements sharing the node i with the node i itself. The number m of stages required to stabilize the second-order RKC method depends on the stiffness of the diffusion term. As derived in [23], we set

$$m = 1 + \left\lceil \left(1 + \frac{\Delta t\, \sigma_J}{0.653} \right)^{\frac{1}{2}} \right\rceil, \tag{25}$$

with σ_J the spectral radius of the Jacobian matrix associated with the space-discrete diffusion operator $\mathbf{F}_{\mathbf{D}}$. In particular, we estimate σ_J with the Gershgorin circle theorem, while we compute numerically the derivatives involved in the definition of the Jacobian matrix. Note that, in applications where the diffusion term is very stiff, the spectral radius may become very large and, consequently, the RKC scheme few effective in practice, since requiring a significant number of internal stages to stabilize. Vice versa, formula (25) preserves a meaning in case of a mildly stiff diffusion operator and severely stiff reaction terms, as for the problem we are dealing with in this paper.

Concerning the several coefficients involved in (24), we adopt the definitions provided in [23], that we supply here for completeness. With this aim, we introduce: the Chebyshev polynomials of the first kind, defined by the recursive relation

$$T_0(x) = 1, \quad T_1(x) = x, \quad T_j(x) = 2xT_{j-1}(x) - T_{j-2}(x), \tag{26}$$

for $2 \leq j \leq m$ and $x \in \mathbb{R}$, where index j keeps trace of the polynomial degree;

the positive real parameter ϵ, known as dumping parameter, that we set to $2/13$ in order to ensure a second order scheme as underlined in [24, 23]; quantities

$$\omega_0 = 1 + \frac{\epsilon}{m^2}, \quad \omega_1 = \frac{T_m^{'}(\omega_0)}{T_m^{''}(\omega_0)}; \quad b_0 = b_1 = b_2, \quad b_j = \frac{T_j^{''}(\omega_0)}{\left[T_j^{'}(\omega_0)\right]^2}.$$

Thus, coefficients $\mu_j, \nu_j, \tilde{\mu}_j, \tilde{\gamma}_j$ and c_j are computed by

$$\mu_j = \tfrac{2b_j\omega_0}{b_{j-1}}, \quad \nu_j = \tfrac{-b_j}{b_{j-2}}, \quad \tilde{\mu}_j = \tfrac{2b_j\omega_1}{b_{j-1}} \quad \text{with } \tilde{\mu}_1 = b_1\omega_1,$$

$$\tilde{\gamma}_j = -(1 - b_{j-1}T_{j-1}(\omega_0))\tilde{\mu}_j, \quad c_j = \tfrac{T_m^{'}(\omega_0)}{T_m^{''}(\omega_0)}\tfrac{T_j^{''}(\omega_0)}{T_j^{'}(\omega_0)} \quad \text{with } c_0 = 0,\ c_1 = \tfrac{c_2}{4\omega_0},$$

with $2 \leq j \leq m$.

We observe that the explicit treatment of the diffusion term in (24) leads to a nonlinear algebraic system of equations that is not coupled in space. Thus, at each mesh node and at each internal stage of the IMEX-RKC method, a single nonlinear equation has to be solved. This represents a key aspect in a parallel implementation, since leading to a fully decoupled system as for the TG2 scheme. Since the mass conservation equation is independent on the diffusion term, the RKC internal stages are performed just for the momentum equation. Furthermore, the bed friction term included in $\mathbf{F_R}$ depends on the x- and y-mass fluxes, separately (see the rheology law in (6)), so that the non-linearity on each mesh node can be tackled with a scalar semi-smooth Newton method along both the x- and y-direction without requiring a matrix inversion. The semi-smooth Newton method adopted is similar to the one described in the works [47, 48, 49] for contact problems. The choice for a semi-smooth scheme is due to the fact that the bed friction is a function of the absolute value of the velocity components thus resulting in a piece-wise differentiable function, and to the presence of a signum function. In particular, we consider a linear relaxation of the signum function in (6) to ensure the piece-wise differentiability. Thus, for $x \in \mathbb{R}$, we replace $\text{sgn}(x)$ with the linear relaxation

$$\text{sgn}_\gamma(x) = \begin{cases} 1 & \text{if } x > \gamma, \\ -1 & \text{if } x < -\gamma, \\ \dfrac{x}{\gamma} & \text{otherwise,} \end{cases} \tag{27}$$

such that $\text{sgn}(x) = \lim_{\gamma \to 0} \text{sgn}_\gamma(x)$, with γ a strictly positive relaxation parameter set to 10^{-2} in the simulation we present here.

The selected time discretization in the presence of a $\mathbb{Q}_1$ spatial finite element

discretization leads to a numerical scheme which is second order in space and time.

3.3. Strang splitting IMEX-RKC TG2-PC method

In this section, we establish the approximation scheme we adopt for the numerical assessment in the next section. The basic remark is that in model (1) the transport and the diffusion-reaction contributions exhibit completely different characteristics from a numerical point of view. This justifies the adoption of a splitting method [8, 7] in order to achieve an efficient integration in time, so that each term can be integrated using the most suitable scheme. In this work, we resort to the Strang splitting which is second-order accurate and strongly stable [8].

To simplify the presentation, we define the transport and the diffusion-reaction continuous operators as $\mathcal{T}(\mathbf{q}) = -\nabla \cdot \mathbf{F} - \mathbf{B}\nabla Z$ and $\mathcal{D}(\mathbf{q}, \nabla\mathbf{q}) = \mathbf{r} - \nabla \cdot \mathbf{G}$, respectively. The Strang splitting method coincides with the following three-step procedure: given $\mathbf{q}^n$,

$$
\begin{aligned}
&\partial_t \mathbf{q}^{(1)} = \mathcal{T}(\mathbf{q}^{(1)}) \quad \text{with } \mathbf{q}^{(1)}(\mathbf{x}, t^n) = \mathbf{q}^n,\\
&\partial_t \mathbf{q}^{(2)} = \mathcal{D}(\mathbf{q}^{(2)}, \nabla\mathbf{q}^{(2)}) \quad \text{with } \mathbf{q}^{(2)}(\mathbf{x}, t^n) = \mathbf{q}^{(1)}\Big(\mathbf{x}, t^n + \frac{\Delta t}{2}\Big),\\
&\partial_t \mathbf{q}^{(3)} = \mathcal{T}(\mathbf{q}^{(3)}) \quad \text{with } \mathbf{q}^{(3)}\Big(\mathbf{x}, t^n + \frac{\Delta t}{2}\Big) = \mathbf{q}^{(2)}(\mathbf{x}, t^n + \Delta t),\\
&\mathbf{q}^{n+1} = \mathbf{q}^{(3)}(\mathbf{x}, t^n + \Delta t),
\end{aligned}
$$

for $n \geq 0$. Then, we integrate the first and third step with the TG2-PC method, while we use the IMEX-RKC finite element scheme for the integration of the second step which involves the stiff reaction-diffusion operator. Hereafter we call this scheme as Split IMEX-RKC TG2-PC method.

Note that, for stability reasons, the complete scheme is only subject to the Courant–Friedrichs–Lewy (CFL) condition of the transport operator. Indeed, the IMEX-RKC finite element scheme is unconditionally stable thus does not require any time step restriction for stability. To this aim, we compute the time step restriction based on the time step Δt. It is then clear that, for stability reasons, the CFL condition can be maximum equal to 2 considering that the first and third step of the Strang splitting procedure advancing of a time step $\frac{\Delta t}{2}$. This constitutes a key difference with respect to the TG2 method [36, 5, 4, 6], where a more restrictive time step is usually necessary to cope with the stiffness of the reaction term as well as to satisfy the time step restriction induced by the diffusion term that scales as h^{-2}, with h the mesh spacing.

4. Numerical results

We present the results of some simulations performed to assess the performance of the numerical scheme presented in the previous section. We will also compare the proposed scheme with a standard explicit TG2 method in terms of computational efficiency, in the context of fast landslides modeling [36, 5, 4, 6]. In more detail, in Section 4.1 we discuss the reliability of the Split IMEX-RKC TG2-PC method, by investigating the accuracy and the well-balancing of the numerical scheme. The efficiency of the implementation is analyzed in Section 4.2, where we present three idealized tests with increasing complexity. Finally, in Section 4.3 we consider a real case study, by resorting to a space wet-dry interface tracking mesh adaptation procedure.

The numerical framework has been implemented using the parallel library, *bim*++ [50, 51, 6], written in C++, which implements partial differential operator discretization, recovery–based error estimators and metric-based mesh adaptation procedures on hierarchical quadtree meshes. In particular, in *bim*++ mesh refinement, coarsening, balancing and partitioning make use of functionalities offered by the library *p4est* [52]. For more details about the adopted space adaptation procedure, the reader can refer to [50, 6]. Concerning the time discretization, we vary the time step based on the Courant–Friedrichs–Lewy (CFL) condition, by setting, if not otherwise stated, the CFL value to 0.9 so that the positivity-preserving constraint on the free surface is guaranteed on the first and third Strang splitting steps. In an example we show results of the proposed discretization method considering a CFL number considerably greater than one.
We define by L_x and L_y respectively the x- and y-extensions of the computational domain Ω.
From a computational viewpoint, we set the threshold, $H_{\min} = 10^{-5}\ m$, on the material height, such that under this threshold we have a null velocity. Finally, as mentioned in Section 3.2, we numerically compute the spectral radius, σ_J, of the Jacobian matrix of the space-discrete diffusive fluxes in (25) needed to provide an estimation of the number of stages required by the RKC scheme. Since the resulting space-discrete diffusion operator is a function of just the momentum fluxes, we consider an increment on U_x and U_y, set to 10^{-8} for both the components. Finally, we perform all the calculations in double precision.

We run the simulations presented in Sections 4.2.2, 4.2.3, 4.3 on the same supercomputer architecture used in [6], the CINECA GALILEO100. In particular, we perform the compilation and linking steps with gcc-10 and OpenMPI $4.1.1$. For all the others experiments we use a laptop with an Intel i7 CPU having 2.60GHz clock frequency and 16GB of RAM.

4.1. Reliability assessment

In the first set of numerical examples, we provide numerical evidence about the accuracy and well-balancing of the Split IMEX-RKC TG2-PC method.

4.1.1. Accuracy tests

In the first test, we provide a simulation of the viscous dam break problem without bed friction. We consider a uniform material height $H = 1\text{m}$, a null initial condition for U_y, and an initial mass flux profile along the x-direction, given by

$$U_x(\mathbf{x}, 0) = \begin{cases} 1 & \text{if } x \leq L/2, \\ 0.5 & \text{if } x > L/2, \end{cases} \tag{28}$$

with $L = L_x = L_y = 5\text{m}$. Here, we set the following simulation parameters $\rho = 1\text{kg/m}^3$, $\mu = 0.05\text{Pa·s}$, $\tau_Y = 0\text{Pa}$, $T = 0.3\text{s}$, $g = 9.81\text{m/s}^2$.

In Figure 3 we show the results of the test by gradually increasing the mesh

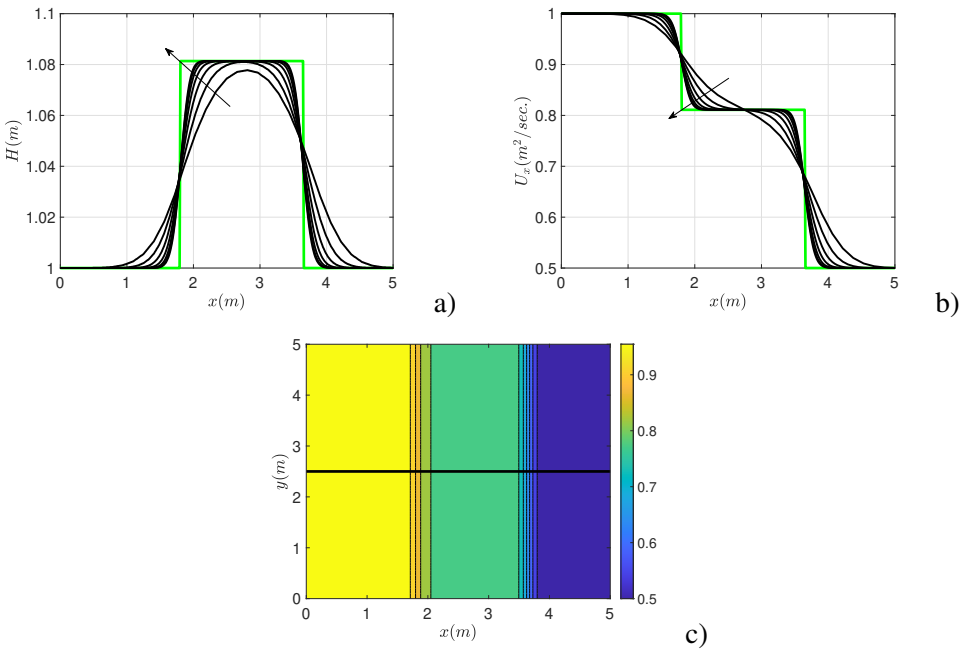

Figure 3: Accuracy tests. Viscous dam-break problem. Panels a), b): comparison between the analytical inviscid solution (in green) and the Split IMEX-RKC TG2-PC viscous solution (in black), for various levels of mesh refinement (the arrows highlight the increasing values of l); Panel c): isolines of H, with black-highlighted the line $y = L_y/2$ along which we compute the one-dimensional solution shown in panels a), b).

refinement. In more detail, if l denotes the refinement level, the number of cells used to discretize the domain in both the x- and y-direction turns out to be equal to 2^l. Panels a), b) gather the analytical inviscid solution (in green) along the line $y = L_y/2$ (see panel c)) and at time T, together with the corresponding Split IMEX-RKC TG2-PC viscous solution (in black), when varying l from 5 to 11. The comparison is carried out in terms of the velocity component U_x (panel a)) and of the material height H (panel b)). As expected, the higher l, the sharper the approximation.

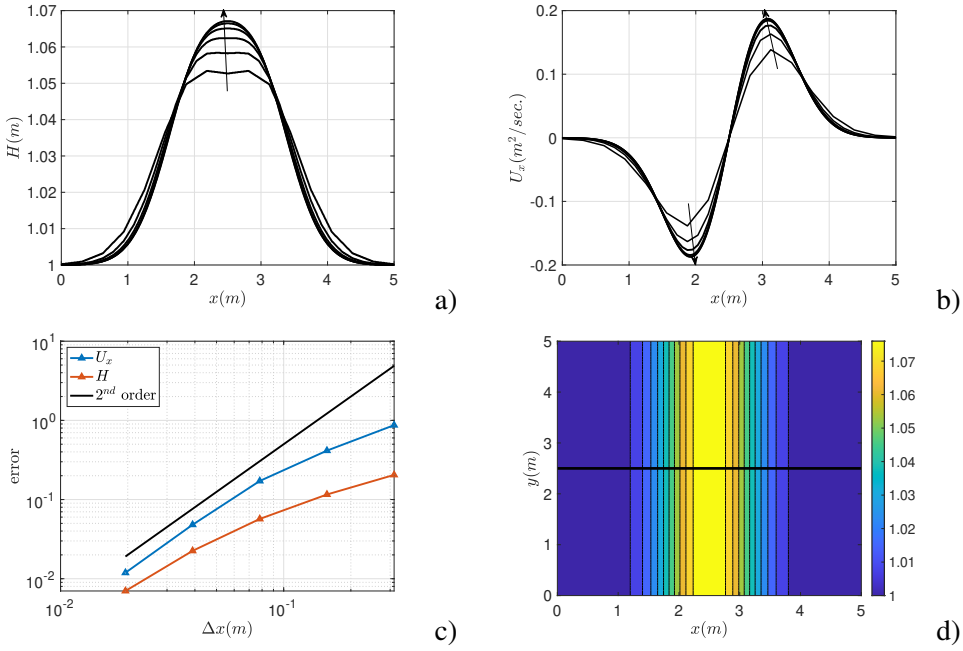

Figure 4: Accuracy tests. Smooth solution. Panels a), b): solutions of the Split IMEX-RKC TG2-PC scheme for various level of mesh refinement (the arrows highlight the increasing values of l); Panel c): convergence trend with respect to $L^2(\Omega)$-norm, where the reference solution refers to $l = 9$; Panel d): isolines of H for $l = 9$, with black-highlighted the line $y = L_y/2$ along which we compute the one-dimensional solution shown in panels a), b).

In a second test, we provide numerical evidence of the expected second-order convergence rate, by considering a smooth configuration. We take into account the smoothly-varying domain identified by the orography profile

$$Z(r) = 1 + \frac{1}{10}\exp\left(-\frac{50}{L^2}r^2\right), \quad \text{with } r^2 = \left(x - \frac{L}{2}\right)^2 \tag{29}$$

and $L = L_x = L_y = 5$m, and we set $\rho = 1$kg/m^3, $\mu = 0.5$Pa·s, $\tau_Y = 0$Pa, $T = 0.1$s, $g = 9.81$m/s^2. We assign a null initial mass flux and

$$H(r, 0) = Z(r) \tag{30}$$

as the initial material profile. We keep the CFL fixed to 0.9 in all the simulations. Finally, we consider a set of refinement levels from 4 to 9. In particular, the $L^2(\Omega)$-norm of the error is computed with respect to the solution associated with the highest level (i.e., $l = 9$).
Figure 4 gathers the results of such a convergence analysis. Panels a), b) provide the Split IMEX-RKC TG2-PC numerical solutions for the different refinement levels, computed along the line $y = L_y/2$ (see panel d)) and at time T. Panel c) displays the convergence trend of the error. We experience a sharp second-order convergence for the mass flux, while the material height reaches a value of 1.68. In Table 1, we collect the number of RKC stages when increasing the number l of refinement levels.

l	4	5	6	7	8	9
#stages RKC	2	3	4	6	9	12

Table 1: Accuracy tests. Smooth solution. Number of stages of the RKC method (#stages RKC) for different values of l.

Finally, in Figure 5 we compare the Split IMEX-RKC TG2-PC scheme with the TG2 method, when varying l from 4 to 8 (we refer to [6] for the specific TG2 scheme used for the comparison). We notice that the two approximate solutions approach each other when refining the mesh, in accordance with the expectations. A comparison between the Split IMEX-RKC TG2-PC and the TG2 approaches will be carried out in terms of CPU time in Section 4.2.

4.1.2. Well-balancing test

The purpose of this test problem is to verify that the Split IMEX-RKC TG2-PC scheme maintains the well-balancing property over a non-flat bottom. With this aim, we consider the same configuration described in [53], namely a domain extension $L = L_x = L_y = 10$m, a final time $T = 0.5$s and two different functions to model the bottom orography, i.e.,

$$Z(\mathbf{x}) = Z_1(\mathbf{x}) = 5e^{-\frac{2}{5}(x-5)^2}, \tag{31}$$

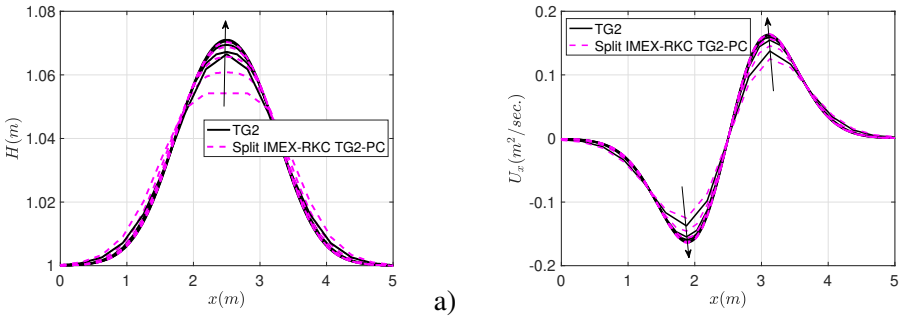

Figure 5: Accuracy tests. Smooth solution. Panels a), b): comparison between the Split IMEX-RKC TG2-PC and the TG2 schemes for various levels of refinement, from 4 to 8.

which is smooth, and

$$Z(\mathbf{x}) = Z_2(\mathbf{x}) = \begin{cases} 4 & \text{if } 4 \leq x \leq 8 \\ 0 & \text{otherwise} \end{cases} \tag{32}$$

characterized by discontinuity. The initial condition coincides with the stationary solution,

$$H + Z(\mathbf{x}) = 10, \quad [U_x, U_y]^\top = \mathbf{0}. \tag{33}$$

This steady-state configuration is expected to be preserved exactly by the numerical scheme. We consider a discretization of the domain with a level of refinement l equal to 8. Table 2 provides the $L^1(\Omega)$- and $L^\infty(\Omega)$-norm of the error associated with the two components of the velocity and the material height for both the considered orographies. All errors are close to the round-off independently of the selected bed profile, thus verifying the well-balancing property of the split IMEX-RKC TG2-PC method.

	$L^1(\Omega)$-norm of the error			$L^\infty(\Omega)$ -norm of the error		
	H	U_x	U_y	H	U_x	U_y
Z_1	1.67e-13	4.87e-12	1.48e-12	8.88e-15	1.77e-13	1.21e-13
Z_2	1.54e-15	2.78e-13	1.52e-13	3.55e-15	4.48e-14	5.76e-14

Table 2: Well-balancing test. $L^1(\Omega)$- and $L^\infty(\Omega)$-norm of the error for the stationary solution in the presence of a smooth and of a discontinuous bed orography.

4.2. Efficiency assessment

In this section we verify the efficiency of the implementation of the Split IMEX-RKC TG2-PC scheme, by comparing the proposed method with the standard TG2 approach [4, 5, 6].
This analysis is performed on three case studies. In the first one, we consider a flat plane and a null yield shear stress τ_Y, i.e., we deal with a Newtonian rheology; in the second test we still have a flat plane, but we consider bed friction with a Bingham fluid [31]; in the last configuration, we analyze the flow of a Bingham fluid with bed friction over an inclined plane orography. The comparison with the TG2 scheme is carried out in terms of time step selection for all the three cases, and of parallel performance for the second and third settings.

4.2.1. Example 1

We consider a flat plane, a null yield shear stress, a frictionless bed, a final simulation time $T = 0.2$s in a square domain with extensions $L = L_x = L_y = 5$m, for both the TG2 and Split IMEX-RKC TG2-PC scheme. We set null initial conditions on the mass fluxes, while selecting as initial material profile,

$$H(r,0) = \begin{cases} 2 & \text{if } r \leq \frac{1}{2}, \\ 1 & \text{if } r > \frac{1}{2}, \end{cases} \tag{34}$$

where r is the radial distance from the barycenter of the square domain Ω, i.e, $r = \sqrt{(x - L/2)^2 + (y - L/2)^2}$. This is equivalent to considering a radial dam break problem with a gravitational field $g = 9.81\text{m/s}^2$, a density $\rho = 1\text{kg/m}^3$ and a fluid viscosity $\mu = 0.1$Pa·s.

Δx	TG2	Split IMEX-RKC TG2-PC	#stages RKC
0.1	$6.86646 \cdot 10^{-3}$	$3.33623 \cdot 10^{-2}$	4
0.05	$1.71661 \cdot 10^{-3}$	$1.63593 \cdot 10^{-2}$	4
0.025	$4.29153 \cdot 10^{-4}$	$8.1052 \cdot 10^{-3}$	6
0.0125	$1.07288 \cdot 10^{-4}$	$4.05579 \cdot 10^{-3}$	8

Table 3: Example 1. Time steps in seconds for the TG2 and for the Split IMEX-RKC TG2-PC method and the number of stages required by the RKC method #stages RKC for the Split IMEX-RKC TG2-PC method, for the different minimum linear resolutions considered Δx.

We consider a space adaptation procedure as described in the work [6] carried out at each time step with a tolerance on the recovery based estimator equal to $\tau =$

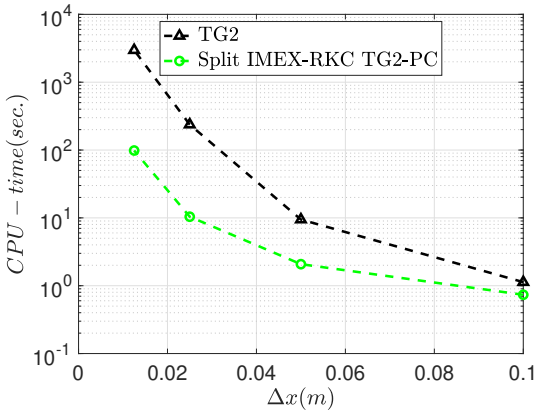

Figure 6: Example 1. Plot of the CPU-time against the resolution Δx for both the TG2 and the Split IMEX-RKC TG2-PC method, the y-axis is in semilogarithmic scale.

10^{-5}m. In particular, we consider a set of minimum linear resolutions in the wet region equal to $\{0.1, 0.05, 0.025, 0.0125\}m$. The numerical results are obtained using 4 processors. We consider a CFL number, which we recall is calculated on the time step Δt, equal to 0.9 and 1.8 on the TG2 and on the Split IMEX-RKC TG2-PC, respectively. In this way, for the Split IMEX-RKC TG2-PC method, we recover a CFL number equal to 0.9 in the single TG2-PC procedure. In Figure 6 and Table 3 we compare the TG2 and the Split IMEX-RKC TG2-PC approaches by providing, for the different linear resolutions considered, the plot of the CPU-time and the time step, respectively. We can observe that the method here proposed enables the use of a considerably larger time step compared to the TG2 method. This reflects also on the CPU-time, which ranges from the almost the same CPU time of the TG2 scheme in case of $\Delta x = 0.1$m to a CPU time that is roughly 3% of the CPU time required by the standard TG2 scheme in case of $\Delta x = 0.0125$m. This is a considerably greater improvement over the standard TG2 method. Finally, in Figure 7, first in panel a) we report the final time mesh in case of $\Delta x = 0.025$m together with the isolines of the material height H and in white the line over which we exctract the one-dimensional solution that we present in panels b), c). There, we show the final time solutions obtained in case of $\Delta x = 0.0125$m by the TG2 and the Split IMEX-RKC TG2-PC method. We particularly note that, the classical TG2 scheme results to be more dissipative than the proposed Split IMEX-RKC TG2-PC approach. Indeed, as one can notice, the Split IMEX-RKC TG2-PC method produces almost the same solution of the most refined solution of the TG2 scheme in case of $\Delta x = 0.05$m and a CFL number equal to 0.2, see the magenta dashed line.

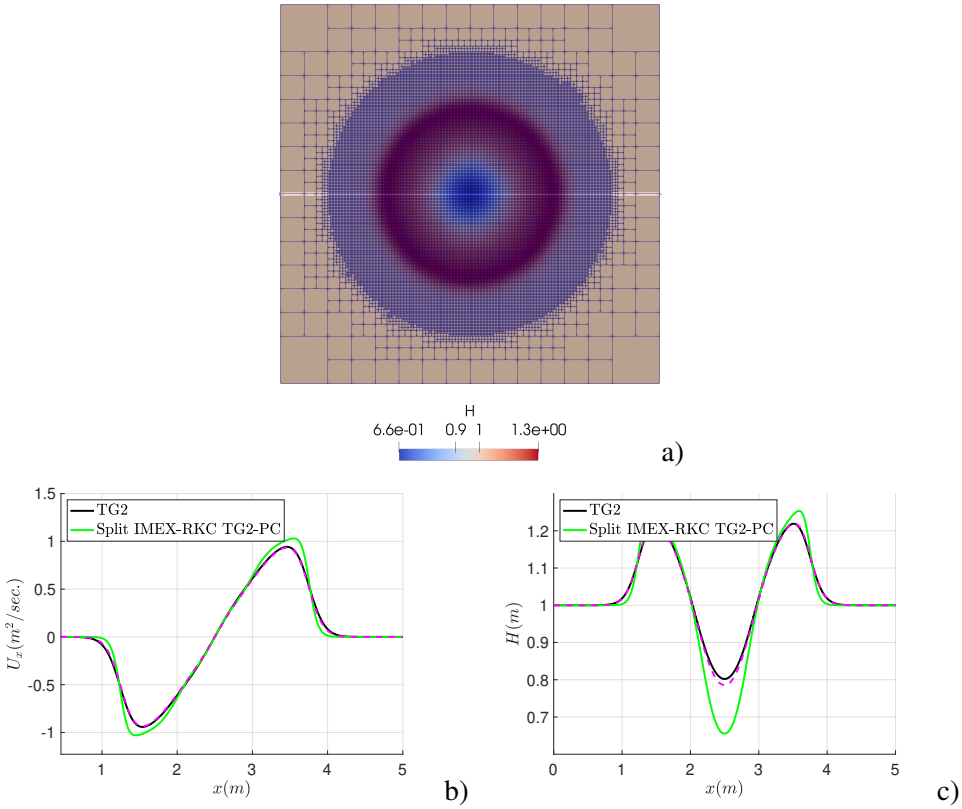

Figure 7: Example 1. a) shows the isolines of the material height together with the mesh and in white the line over which we extract the one-dimensional solution we present in panels b), c); b), c) final time mass flux and material height for the TG2 and the Split IMEX-RKC TG2-PC methods. The magenta dashed line is the solution obtained by the Split IMEX-RKC TG2-PC in case of $\Delta x = 0.05$m and a CFL number equal to 0.2.

4.2.2. Example 2

We consider the same configuration as in the previous section. We change the following simulation parameters, $\rho = 1300\text{kg/m}^3$, $\mu = 50\text{Pa·s}$, and we consider a Bingham fluid with $\tau_Y = 10^3\text{Pa}$.

In Figure 8 we show some results of the simulation obtained with a level of refinement $l = 10$, which corresponds to a space resolution of roughly $5 \cdot 10^{-3}$m in both directions. In particular, panels a), b) provide the trend of the material height and of the mass flux extracted along the x-direction at the final time T. The numerical scheme is capable of detecting both the rarefaction and the shock waves. Panels c), d) collect computational information, namely, the number of RKC stages against time and the speedup gained when increasing the number of processors,

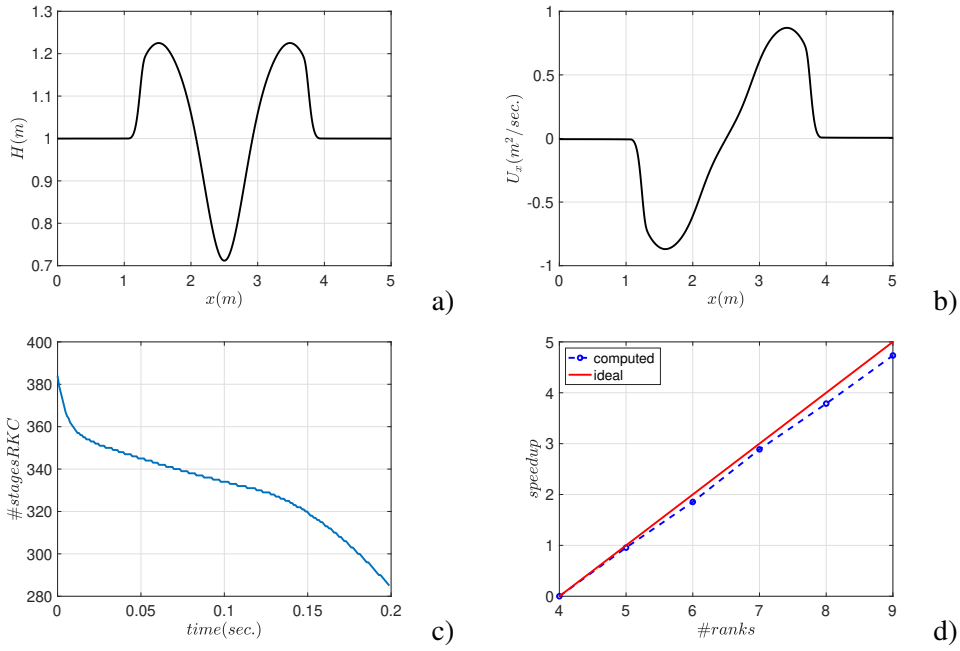

Figure 8: Example 2. a) Material height and b) mass flux along the x-direction at the final time; c) RKC number of stages against time; d) speedup of the strong scaling analysis in a `log2-log2` plot.

from 16 to 512. We reach a parallel efficiency around 80%, even though we have over 300 RKC number of stages for all the simulation time. This confirms the efficiency of the implementation since the RKC method is a completely data-local method, and the number of RKC stages does not affect the parallel performances.

4.2.3. Example 3

This example involves a granular sliding mass along a planar orography profile so that the source term plays a role. The slope of the profile is approximately equal to $22°$ along the x axis. We choose the following parameters: gravitational field $g = 9.81\text{m/s}^2$, simulation time $T = 5\text{s}$, density $\rho = 1400$ kg/m^3, viscosity $\mu = 50\text{Pa·s}$, yield shear stress $\tau_Y = 2 \cdot 10^3\text{Pa}$, turbulent coefficient $\xi = 10\text{m/s}^2$, bed friction angle $\delta = 23°$, $p_S = 0\text{Pa}$, domain extension $L = L_x = L_y = 1000\text{m}$. We consider a material initially at rest, with an initial height

$$H(\mathbf{x}, 0) = \begin{cases} \max\{0, \min\{500x/L - 200, 30\}\} & \text{for } \mathbf{x} \in V, \\ 0 & \text{otherwise,} \end{cases} \tag{35}$$

where

$$V = \left\{ \mathbf{x} \in \mathbb{R}^2 : \frac{(x - L/2)^2}{L^2} + \frac{(x - L/2)^2}{L^2} \leq \left[0.2 + 0.01 \sin\left(10 \frac{y - L/2}{L} \frac{\pi}{L} \right) \right]^2 \right\}.$$

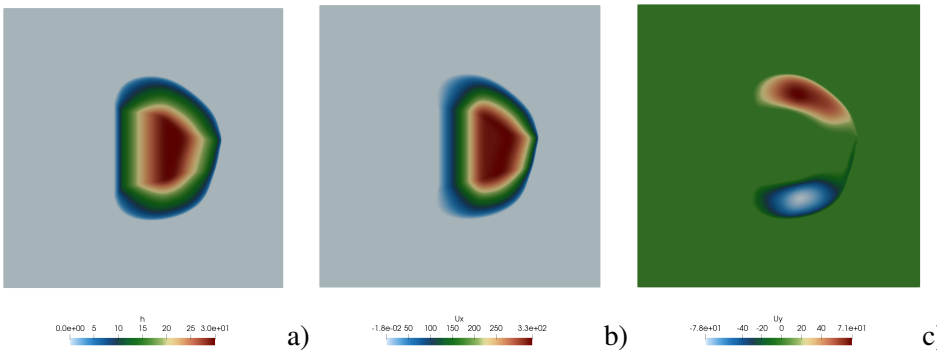

Figure 9: Example 3. a) Material height, b) x- and c) y-direction mass flux distribution in Ω at the final time.

We adopt a space discretization with a level l of refinement equal to 10. Figure 9 offers qualitative results of the simulation, by providing the spatial distribution of the material height and of the x- and y-direction mass flux (from the left to the right panel) at time T. It is evident the absence of the slope contribution in panel c), while in panel b) we detect an offset due to the presence of the slope along the x-direction. Figure 10 provides more quantitative information related to the numerical algorithm, namely the number of RKC stages against time in panel a), the time step size against time in panel b), the plot of the absolute stability region for three different numbers of stages in panel c), and the speedup of a strong scaling analysis using a number of processors from 16 to 512 in panel d). The RKC number of stages, as well as the time step, are decreasing during the simulation. This is compliant with the expectation since the problem is stiffer during the first movement of the material; then, the transport fluxes assume more importance leading to an advection-dominated setting. Panel c) highlights the increment of the stability region when increasing the value of m. Regarding the speedup, we obtain a parallel efficiency around 80%, analogously as for the previous test case.

4.3. A real case study

We focus now on a real case study simulation to show the capability of the Split IMEX-RKC TG2-PC method to deal with real problems. We will prove that the

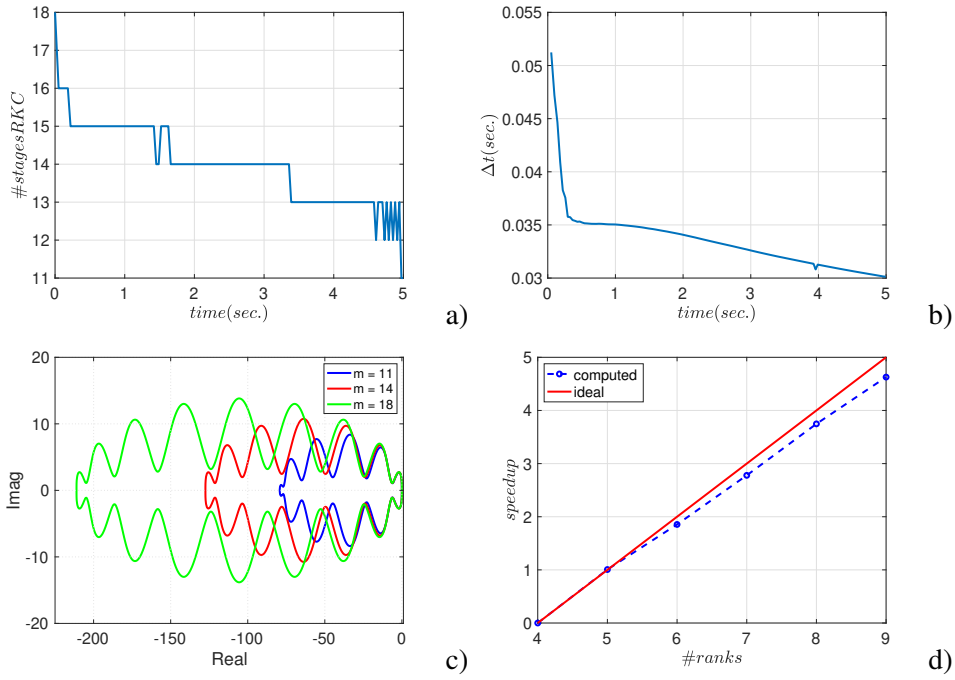

Figure 10: Example 3. a) RKC number of stages against time; b) time step against time; c) absolute stability region for a different number m of stages; d) speedup of the scaling analysis in a `log2-log2` plot.

implemented algorithm ensures some strong scaling results when set in the space-time adaptive framework with quadtree interface tracking described in [6], where mesh adaptation is driven by material height.

We consider the Bindo-Cortenova case study, namely a wide translational landslide, located in Valsassina (Lecco province, Lombardy, Italy) that underwent a catastrophic failure in December 2002 (volume ca $1.2 \cdot 10^6$m^3). We refer to [54] for a complete explanation of the involved geological aspects. The 5m-resolution Digital Terrain Model (DTM) with domain extent $L_x = 820$m, $L_y = 870$m is furnished, together with the corresponding slope, in Figure 11, the mean slope angle being approximately equal to $28°$. According to [55], the average thickness of the slide is assumed to be equal to 38m, the material density is $\rho = 1291$kg/m^3, the bed friction angle is $\delta = 33.9°$ and the surface pressure is $p_S = 1$atm. Regarding the Bingham and Voellmy rheological models, we set the following coefficients $\mu = 50$Pa·s, $\tau_Y = 2 \cdot 10^3$Pa, $\xi = 10^3$m/s^2. We select a final time $T = 10$s, a cell resolution of 0.25m in wet-dry interface regions and a 1m minimum resolution in wet regions. Finally, the space adaptation is carried out every 0.5s, with a tolerance

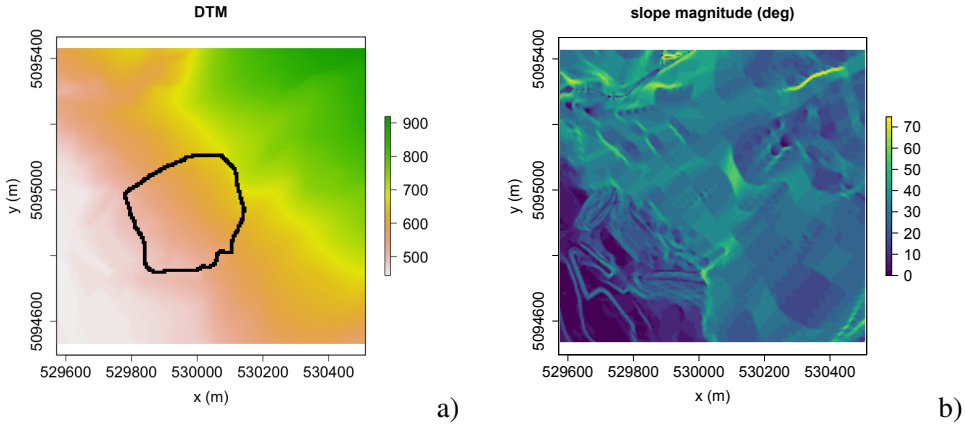

Figure 11: Real case study. a) Isolines of the DTM together with its corresponding slope magnitude in degrees b).

on the recovery based estimator equal to $\tau = 10^{-5}$m (we refer to [6] for further details).

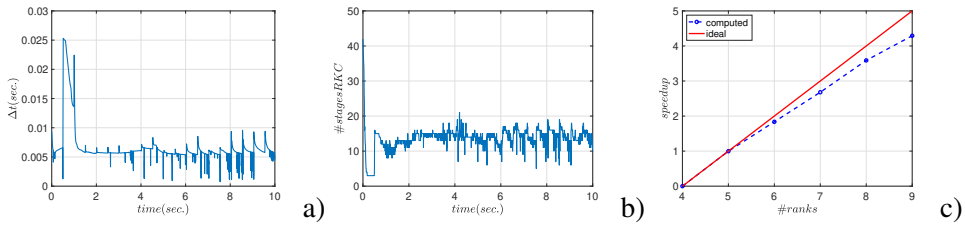

Figure 12: Real case study. Evolution of a) the time step and b) of the RKC number of stages as a function of time; c) speedup of the scaling analysis in a `log2-log2` plot.

Figure 12 shows the time evolution of the time step (panel a)) and of the number of stages of the RKC method (panel b)), together with the speedup characterizing the scaling analysis from 16 to 512 processors. The trend of Δt exhibits several peaks in correspondence with the spatial adaptation phases, although, on average, the behaviour is very similar to the one in Figure 10 where, after the initial movement of the material, the time step tends to reach a constant state when the landslide behaves similarly to a Newtonian fluid. The oscillatory plot of the time step finds a counterpart in the evolution characterizing the RKC number of stages. We note that the maximum number of mesh nodes is of the order of half a million. This results into a lower speedup (ranging between 60% and 70%) when compared with the cases presented in the previous sections.
Finally, in Figure 13, we provide some sketches of the solution at the final time. In

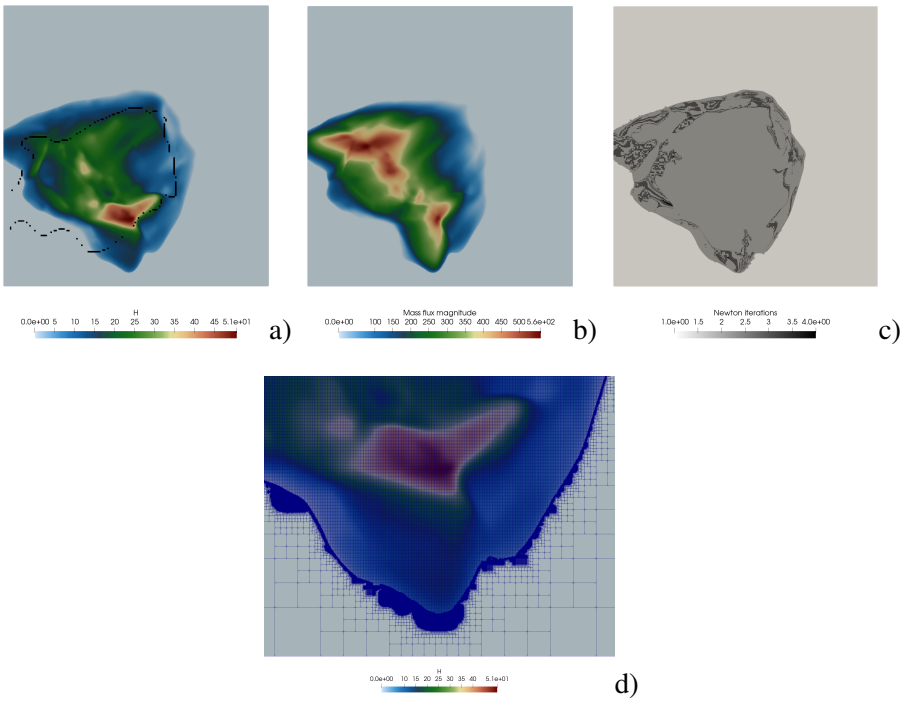

Figure 13: Real case study. a) Material height and b) absolute value of the mass flux distribution at time T; c) Newton iterations of the IMEX-RKC at the final stage and d) detail of the adapted mesh at time T.

more detail, panel a) displays the material height colormap with, in black, the line representing the final landslide material deposition according to geological observations; panel b) provides the absolute value of the mass flux distribution; panel c) shows the isolines of the Newton iterations at the final stage of the RKC method; panel d) offers an enlarged view of the adapted mesh overlapped to the material height distribution. Panels a) and b) show that the landslide is reaching a steady state (as confirmed by the small values of $|\mathbf{U}|$ along the falling mass boundary) in contrast to, for instance, the configuration in Figure 9. This has an impact on the small number (up to 4) of iterations demanded by the Newton scheme to converge. Finally, we note the detection of the wet-dry interface guaranteed by the front-tracking methodology fully described in [6].

5. Conclusions

We have proposed an efficient parallel second-order well-balanced space-time numerical framework for simulating the run-out phase of rapid landslides.

The method is characterized by a larger stability region when compared with the standard TG2 scheme while preserving the locality of the implementation. The new method, which we name Split IMEX-RKC TG2-PC, combines the TG2-PC discretization with the IMEX-RKC approach through an operator-splitting strategy. We have applied the Split IMEX-RKC TG2-PC scheme to the solution of the single-phase depth-integrated model for fast-moving landslides, and showed it to be exact when dealing with the lake-at-rest steady state solution. In particular, the new numerical framework offers a more efficient tool when compared with the standard TG2 method in the approximation of the single-phase model for the run-out phase of fast-moving landslides.
The Split IMEX-RKC TG2-PC method has been numerically assessed in case of both idealized and real DTM orography configurations. In particular, after some reliability tests showing the accuracy and the numerical evidence of the well-balancing property of the numerical scheme, we have carried out some comparisons against the TG2 method in terms of time step selection and parallel performance and provided strong scaling results to show the efficiency of the parallel implementation.

As for possible future developments, we mention the possibility of exploiting the scalability of our code to perform simulation intensive tasks such as an uncertainty quantification analysis applied to a real landslide run-out. This could be performed, for instance, by using methods like the polynomial chaos expansion [56]. We also plan the extension of the proposed numerical simulation framework to include the landslide initiation phase dynamics. This implies the addition of the consolidation time process in the numerical model, which is the principal responsible of long-term landslide dynamics.

Acknowledgements

This research was supported by the Accordo Attuativo ASI-POLIMI "Attività di Ricerca e Innovazione" n. 2018-5-HH.0.

C.d.F. and L.F. have been partially funded by the Italian Research Center on High-Performance Computing, Big Data and Quantum Computing (ICSC), European Union - Next Generation EU.

The present research is within the framework of the project "Dipartimento di Eccellenza 2023-2027" granted by Italian MUR.

We thank the anonymous reviewer for helping to improve the quality of the manuscript.

Conflict of interest

The authors declare that they have no potential conflict of interest.

References

[1] J. Donea, A Taylor–Galerkin method for convective transport problems, International Journal for Numerical Methods in Engineering 20 (1) (1984) 101–119.

[2] R. Löhner, K. Morgan, O. C. Zienkiewicz, The solution of non-linear hyperbolic equation systems by the finite element method, International Journal for Numerical Methods in Fluids 4 (11) (1984) 1043–1063.

[3] B. V. K. S. Sai, O. C. Zienkiewicz, M. T. Manzari, P. R. M. Lyra, K. Morgan, General purpose versus special algorithms for high-speed flows with shocks, International Journal for Numerical Methods in Fluids 27 (1-4) 57–80.

[4] M. Quecedo, M. Pastor, A reappraisal of Taylor–Galerkin algorithm for drying–wetting areas in shallow water computations, International Journal for Numerical Methods in Fluids 38 (6) (2002) 515–531.

[5] M. Quecedo, M. Pastor, M. I. Herreros, J. A. Fernández Merodo, Numerical modelling of the propagation of fast landslides using the finite element method, International Journal for Numerical Methods in Engineering 59 (6) (2004) 755–794.

[6] F. Gatti, M. Fois, S. Perotto, C. de Falco, L. Formaggia, Parallel simulations for fast-moving landslides: space-time mesh adaptation and sharp tracking of the wetting front, to appear in International Journal for Numerical Methods in Fluids (2023). doi:10.1002/fld.5186.

[7] G. I. Marchuk, Some application of splitting-up methods to the solution of mathematical physics problems, Aplikace Matematiky 13 (2) (1968) 103–132.

[8] G. Strang, On the construction and comparison of difference schemes, SIAM Journal on Numerical Analysis 5 (3) (1968) 506–517.

[9] G. Dal Maso, P. G. Lefloch, F. Murat, Definition and weak stability of nonconservative products, Journal de mathématiques pures et appliquées 74 (6) (1995) 483–548.

[10] C. Parés, Numerical methods for nonconservative hyperbolic systems: a theoretical framework., SIAM Journal on Numerical Analysis 44 (1) (2006) 300–321.

[11] M. J. Castro, E. D. Fernández-Nieto, A. M. Ferreiro, J. A. García-Rodríguez, C. Parés, High order extensions of roe schemes for two-dimensional nonconservative hyperbolic systems, Journal of Scientific Computing 39 (1) (2009) 67–114.

[12] M. Castro, J. M. Gallardo, J. A. López-GarcÍa, C. Parés, Well-balanced high order extensions of godunov's method for semilinear balance laws, SIAM Journal on Numerical Analysis 46 (2) (2008) 1012–1039.

[13] J. M. Gallardo, C. Parés, M. Castro, On a well-balanced high-order finite volume scheme for shallow water equations with topography and dry areas, Journal of Computational Physics 227 (1) (2007) 574–601.

[14] M. L. Muñoz-Ruiz, C. Parés, Godunov method for nonconservative hyperbolic systems, ESAIM: Mathematical Modelling and Numerical Analysis 41 (1) (2007) 169–185.

[15] M. Castro, A. Pardo, C. Parés, E. Toro, On some fast well-balanced first order solvers for nonconservative systems, Mathematics of computation 79 (271) (2010) 1427–1472.

[16] M. Dumbser, M. Castro, C. Parés, E. F. Toro, Ader schemes on unstructured meshes for nonconservative hyperbolic systems: Applications to geophysical flows, Computers & Fluids 38 (9) (2009) 1731–1748.

[17] M. Dumbser, D. S. Balsara, A new efficient formulation of the hllem riemann solver for general conservative and non-conservative hyperbolic systems, Journal of Computational Physics 304 (2016) 275–319.

[18] M. Dumbser, A. Hidalgo, M. Castro, C. Parés, E. F. Toro, Force schemes on unstructured meshes ii: Non-conservative hyperbolic systems, Computer Methods in Applied Mechanics and Engineering 199 (9-12) (2010) 625–647.

[19] M. Castro, J. Gallardo, C. Parés, High order finite volume schemes based on reconstruction of states for solving hyperbolic systems with nonconservative products. applications to shallow-water systems, Mathematics of computation 75 (255) (2006) 1103–1134.

[20] M. Dumbser, E. F. Toro, A simple extension of the osher riemann solver to non-conservative hyperbolic systems, Journal of Scientific Computing 48 (1) (2011) 70–88.

[21] F. Fambri, M. Dumbser, S. Köppel, L. Rezzolla, O. Zanotti, Ader discontinuous galerkin schemes for general-relativistic ideal magnetohydrodynamics, Monthly Notices of the Royal Astronomical Society 477 (4) (2018) 4543–4564.

[22] S. Busto, M. Dumbser, S. Gavrilyuk, K. Ivanova, On thermodynamically compatible finite volume methods and path-conservative ader discontinuous galerkin schemes for turbulent shallow water flows, Journal of Scientific Computing 88 (1) (2021) 28.

[23] J. G. Verwer, B. P. Sommeijer, An Implicit-Explicit Runge-Kutta-Chebyshev Scheme for Diffusion-Reaction Equations, SIAM Journal on Scientific Computing 25 (5) (2004) 1824–1835.

[24] J. G. Verwer, W. Hundsdorfer, B. P. Sommeijer, Convergence properties of the Runge-Kutta-Chebyshev method, Numerische Mathematik 57 (1) (1990) 157–178.

[25] B. P. Sommeijer, L. F. Shampine, J. G. Verwer, RKC: An explicit solver for parabolic PDEs, Journal of Computational and Applied Mathematics 88 (2) (1998) 315–326.

[26] R. Bermejo, J. Carpio, An adaptive finite element semi-Lagrangian implicit–explicit Runge–Kutta–Chebyshev method for convection dominated reaction–diffusion problems, Applied Numerical Mathematics 58 (1) (2008) 16–39.

[27] R. Bermejo, P. G. del Sastre, An implicit-explicit Runge-Kutta-Chebyshev finite element method for the nonlinear Lithium-ion battery equations, Applied Mathematics and Computation 361 (2019) 398–420.

[28] M. B. Abbott, Computational Hydraulics: Elements of the Theory of Free Surface Flows, Pitman, London, 1979.

[29] A. Franci, M. Cremonesi, U. Perego, G. Crosta, E. Oñate, 3D simulation of Vajont disaster. Part 1: Numerical formulation and validation, Engineering Geology 279 (2020) 105854.

[30] M. Pastor, T. Blanc, B. Haddad, V. Drempetic, M. Mories, P. Stickle, M. Mira, J. Merodo, Depth averaged models for fast landslide propagation: mathematical, rheological and numerical aspects, Archive of Computational Methods in Engineering 22 (2015) 67–104.

[31] T. C. Papanastasiou, Flows of materials with yield, Journal of rheology 31 (5) (1987) 385–404.

[32] A. Franci, M. Cremonesi, U. Perego, E. Oñate, G. Crosta, 3D simulation of Vajont disaster. Part 2: Multi-failure scenarios, Engineering Geology 279 (2020) 105856.

[33] R. J. LeVeque, Balancing source terms and flux gradients in high-resolution Godunov methods: the quasi-steady wave-propagation algorithm, Journal of Computational Physics 146 (1) (1998) 346–365.

[34] O. Gourgue, R. Comblen, J. Lambrechts, T. Kärnä, V. Legat, E. Deleersnijder, A flux-limiting wetting–drying method for finite-element shallow-water models, with application to the scheldt estuary, Advances in Water Resources 32 (12) (2009) 1726–1739.

[35] J. Qiu, M. Dumbser, C.-W. Shu, The discontinuous Galerkin method with Lax–Wendroff type time discretizations, Computer methods in applied mechanics and engineering 194 (42-44) (2005) 4528–4543.

[36] M. Pastor, M. Quecedo, J. Fernández Merodo, M. Herrores, E. Gonzalez, P. Mira, Modelling tailings dams and mine waste dumps failures, Geotechnique 52 (8) (2002) 579–591.

[37] D. Givoli, Non-reflecting boundary conditions, Journal of computational physics 94 (1) (1991) 1–29.

[38] O. C. Zienkiewicz, K. Morgan, Finite elements and approximation, Courier Corporation, 2006.

[39] M. J. Castro, P. G. LeFloch, M. L. Muñoz-Ruiz, C. Parés, Why many theories of shock waves are necessary: Convergence error in formally path-consistent schemes, Journal of Computational Physics 227 (17) (2008) 8107–8129.

[40] S. Rhebergen, O. Bokhove, J. J. van der Vegt, Discontinuous galerkin finite element methods for hyperbolic nonconservative partial differential equations, Journal of Computational Physics 227 (3) (2008) 1887–1922.

[41] R. Abgrall, S. Karni, A comment on the computation of non-conservative products, Journal of Computational Physics 229 (8) (2010) 2759–2763.

[42] J. Peraire, A finite element method for convection dominated flows, Ph.D. thesis, University College of Swansea, Swansea (1986).

[43] S. T. Zalesak, Fully multidimensional flux-corrected transport algorithms for fluids, Journal of Computational Physics 31 (3) (1979) 335–362.

[44] J. P. Boris, D. L. Book, Flux-corrected transport. iii. Minimal-error FCT algorithms, Journal of Computational Physics 20 (4) (1976) 397–431.

[45] D. Kuzmin, M. Möller, S. Turek, High-resolution FEM–FCT schemes for multidimensional conservation laws, Computer Methods in Applied Mechanics and Engineering 193 (45-47) (2004) 4915–4946.

[46] Y. Xing, X. Zhang, C.-W. Shu, Positivity-preserving high order well-balanced discontinuous Galerkin methods for the shallow water equations, Advances in Water Resources 33 (12) (2010) 1476–1493.

[47] B. Wohlmuth, Variationally consistent discretization schemes and numerical algorithms for contact problems, Acta Numerica 20 (2011) 569–734.

[48] R. L. Berge, I. Berre, E. Keilegavlen, J. M. Nordbotten, B. Wohlmuth, Finite volume discretization for poroelastic media with fractures modeled by contact mechanics, International Journal for Numerical Methods in Engineering 121 (4) (2020) 644–663.

[49] L. Formaggia, F. Gatti, S. Zonca, An XFEM/DG approach for fluid-structure interaction problems with contact, Applications of Mathematics 66 (2) (2021) 183–211.

[50] P. C. Africa, Scalable adaptive simulation of organic thin-film transistors, PhD Thesis in Mathematical Models and Methods in Engineering, Politecnico di Milano, Milano, Italy (2019).

[51] P. C. Africa, S. Perotto, C. de Falco, Scalable Recovery-based adaptation on Quadtree Meshes for Advection-Diffusion-Reaction Problems, arXiv (2022).

[52] C. Burstedde, L. C. Wilcox, O. Ghattas, p4est: Scalable algorithms for parallel adaptive mesh refinement on forests of octrees, SIAM Journal on Scientific Computing 33 (3) (2011) 1103–1133.

[53] Y. Xing, C.-W. Shu, A new approach of high order well-balanced finite volume WENO schemes and discontinuous Galerkin methods for a class of hyperbolic systems with source terms, Comput. Phys 1 (1) (2006) 100–134.

[54] C. Margottini, P. Canuti, K. Sassa, Landslide Science and Practice: Volume 3: Spatial Analysis and Modelling, Vol. 3, Springer Science & Business Media, 2013.

[55] M. M. Secondi, G. Crosta, C. di Prisco, G. Frigerio, P. Frattini, F. Agliardi, Landslide motion forecasting by a dynamic visco-plastic model, in: Landslide science and practice, Springer, 2013, pp. 151–159.

[56] B. Sudret, Global sensitivity analysis using polynomial chaos expansions, Reliability engineering & system safety 93 (7) (2008) 964–979.

MOX Technical Reports, last issues

Dipartimento di Matematica
Politecnico di Milano, Via Bonardi 9 - 20133 Milano (Italy)

10/2023 Corti, M.; Antonietti, P.F.; Bonizzoni, F.; Dede', L., Quarteroni, A.
Discontinuous Galerkin Methods for Fisher-Kolmogorov Equation with Application to Alpha-Synuclein Spreading in Parkinson's Disease

09/2023 Buchwald, S.; Ciaramella, G.; Salomon, J.
Gauss-Newton oriented greedy algorithms for the reconstruction of operators in nonlinear dynamics

08/2023 Bonizzoni, F.; Hu, K.; Kanschat, G.; Sap, D.
Discrete tensor product BGG sequences: splines and finite elements

07/2023 Garcia-Contreras, G.; Còrcoles, J.; Ruiz-Cruz, J.A.; Oldoni, M; Gentili, G.G.; Micheletti, S.; Perotto, S.
Advanced Modeling of Rectangular Waveguide Devices with Smooth Profi les by Hierarchical Model Reduction

06/2023 Artoni, A.; Antonietti, P. F.; Mazzieri, I.; Parolini, N.; Rocchi, D.
A segregated finite volume - spectral element method for aeroacoustic problems

05/2023 Fumagalli, I.; Vergara, C.
Novel approaches for the numerical solution of fluid-structure interaction in the aorta

04/2023 Quarteroni, A.; Dede', L.; Regazzoni, F.; Vergara, C.
A mathematical model of the human heart suitable to address clinical problems

02/2023 Boon, W. M.; Fumagalli, A.; Scotti, A.
Mixed and multipoint finite element methods for rotation-based poroelasticity

03/2023 Africa, P.C.; Perotto, S.; de Falco, C.
Scalable Recovery-based Adaptation on Quadtree Meshes for Advection-Diffusion-Reaction Problems

01/2023 Zingaro, A.; Bucelli, M.; Piersanti, R.; Regazzoni, F.; Dede', L.; Quarteroni, A.
An electromechanics-driven fluid dynamics model for the simulation of the whole human heart